



AFRL-OSR-VA-TR-2014-0261

LIGHT-WEIGHT LOW-LOSS DIELECTRIC POLYMER COMPOSITES CONTAINING CARBON NANOSTRUCT

James Tour
WILLIAM MARSH RICE UNIV HOUSTON TX

10/17/2014
Final Report

DISTRIBUTION A: Distribution approved for public release.

Air Force Research Laboratory
AF Office Of Scientific Research (AFOSR)/ RTD
Arlington, Virginia 22203
Air Force Materiel Command

REPORT DOCUMENTATION PAGE				Form Approved OMB No. 0704-0188	
Public reporting burden for this collection of information is estimated to average 1 hour per response, including the time for reviewing instructions, searching existing data sources, gathering and maintaining the data needed, and completing and reviewing this collection of information. Send comments regarding this burden estimate or any other aspect of this collection of information, including suggestions for reducing this burden to Department of Defense, Washington Headquarters Services, Directorate for Information Operations and Reports (0704-0188), 1215 Jefferson Davis Highway, Suite 1204, Arlington, VA 22202-4302. Respondents should be aware that notwithstanding any other provision of law, no person shall be subject to any penalty for failing to comply with a collection of information if it does not display a currently valid OMB control number. PLEASE DO NOT RETURN YOUR FORM TO THE ABOVE ADDRESS.					
1. REPORT DATE (DD-MM-YYYY) 14-10-2014		2. REPORT TYPE Final Report		3. DATES COVERED (From - To) August 1, 2009 to July 31, 2014	
4. TITLE AND SUBTITLE LIGHT-WEIGHT LOW-LOSS DIELECTRIC POLYMER COMPOSITES CONTAINING CARBON NANOSTRUCTURE				5a. CONTRACT NUMBER	
				5b. GRANT NUMBER FA9550-09-1-0581	
				5c. PROGRAM ELEMENT NUMBER	
6. AUTHOR(S) James M. Tour				5d. PROJECT NUMBER	
				5e. TASK NUMBER	
				5f. WORK UNIT NUMBER	
7. PERFORMING ORGANIZATION NAME(S) AND ADDRESS(ES) William Marsh Rice University 6100 Main St MS 16 Houston, Texas 77005				8. PERFORMING ORGANIZATION REPORT NUMBER Air Force Office of Science and Research	
9. SPONSORING / MONITORING AGENCY NAME(S) AND ADDRESS(ES) Air Force Office of Science and Research 875 Randolph Street Suite 325 Room 3112 Arlington, VA 22203				10. SPONSOR/MONITOR'S ACRONYM(S) AFOSR	
				11. SPONSOR/MONITOR'S REPORT NUMBER(S)	
12. DISTRIBUTION / AVAILABILITY STATEMENT					
13. SUPPLEMENTARY NOTES					
14. ABSTRACT We report that conductive films made from hexadecylated graphene nanoribbons (HD-GNRs) can have high transparency to radiofrequency (RF) waves even at very high incident power density. Nanoscale-thick HD-GNR films with an area of several square centimeters were found to transmit up to 390 W (2 × 105 W/m2) of RF power with negligible loss, at an RF transmittance of ~99%. The HD-GNR films conformed to electromagnetic skin depth theory, which effectively accounts for the RF transmission. The HD-GNR films also exhibited sufficient optical transparency for tinted glass applications, with efficient voltage-induced deicing of surfaces. The dispersion of the HD-GNRs afforded by their edge functionalization enables spray , spin- or blade-coating on almost any substrate, thus facilitating flexible, conformal and large-scale film production. In addition to use in antennas and radomes where RF transparency is crucial, these capabilities bode well for the use of the HD-GNR films in automotive and general glass applications where both optical and RF transparencies are desired.					
15. SUBJECT TERMS					
16. SECURITY CLASSIFICATION OF:			17. LIMITATION OF ABSTRACT	18. NUMBER OF PAGES	19a. NAME OF RESPONSIBLE PERSON ames M. Tour
a. REPORT	b. ABSTRACT	c. THIS PAGE			19b. TELEPHONE NUMBER (include area code) 713-348-6246

Final Technical Report

Project Title: LIGHT-WEIGHT LOW-LOSS DIELECTRIC POLYMER COMPOSITES CONTAINING CARBON NANOSTRUCTURE

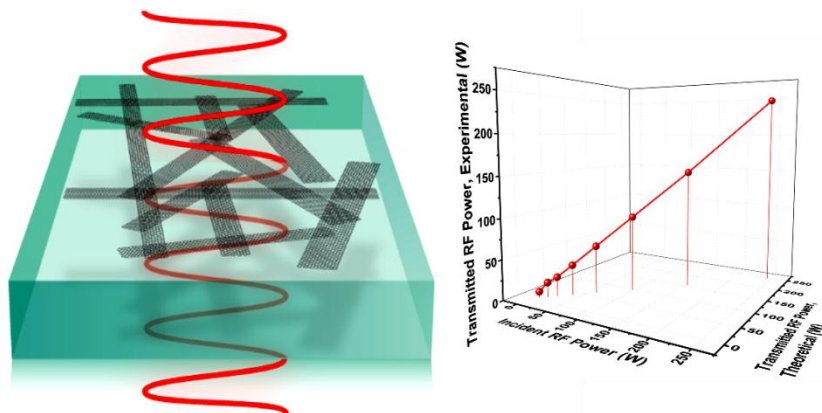
James M. Tour, PI, Rice University

Grant Number: FA9550-09-1-0581

Period Starting: 8/1/2009

Period Ending: 7/31/2014

Functionalized Graphene Nanoribbon Films as a Radiofrequency and Optically Transparent Material



Executive Summary We report that conductive films made from hexadecylated graphene nanoribbons (HD-GNRs) can have high transparency to radiofrequency (RF) waves even at very high incident power density. Nanoscale-thick HD-GNR films with an area of several square centimeters were found to transmit up to 390 W (2×10^5 W/m²) of RF power with negligible loss, at an RF transmittance of ~99%. The HD-GNR films conformed to electromagnetic skin depth theory, which effectively accounts for the RF transmission. The HD-GNR films also exhibited sufficient optical transparency for tinted glass applications, with efficient voltage-induced deicing of surfaces. The dispersion of the HD-GNRs afforded by their edge functionalization enables spray-, spin- or blade-coating on almost any substrate, thus facilitating flexible, conformal and large-scale film production. In addition to use in antennas and radomes where RF transparency is crucial, these capabilities bode well for the use of the HD-GNR films in automotive and general glass applications where both optical and RF transparencies are desired.

Introduction

Radiofrequency (RF) transmissions are used in a wide range of communication applications such as antennas and radomes, mobile services and global positioning systems. We recently reported RF-transparent, electrically conductive hexadecylated graphene nanoribbon (HD-GNR) films for targeted voltage-induced deicing of RF equipment such as radar domes (radomes) and phased array antennas.¹ A large-scale HD-GNR composite film fabrication was demonstrated by spray-coating HD-GNRs on a polymer substrate whereby the HD-GNRs were embedded in polyurethane atop a polyimide flexible substrate rendering a black and optically opaque film. The HD-GNR films were transparent to RF and they transmitted up to 20 W ($7 \times 10^3 \text{ W/m}^2$) of average RF power without significant loss. However, at $> 7 \times 10^3 \text{ W/m}^2$ of average RF power density, there was some RF absorbance localized at thicker spots on the HD-GNR film that caused local increases in temperature. Subsequent thermal breakdown and carbonization of the polyurethane coating and polyimide substrate significantly reduced the RF transmittance. Thus fabrication of highly uniform HD-GNR films would enhance RF transparency.

Though HD-GNRs films are not continuous films, they are composed of a percolating network of ribbons without any thick aggregates or random thick regions. Strong optical and RF absorption can occur on film surfaces where there are thicker regions and contaminants.²⁻⁴ Although conductive carbon-based thin films have been heavily studied,⁵⁻⁸ there is a lack of reports on conductive carbon-based films that are highly transparent to RF. Previous studies have reported on the electromagnetic shielding properties of carbon-based^{9,10} and metal nanowire^{11,12} films and composites in the RF/microwave region where the materials absorb a significant amount of the electromagnetic radiation. The HD-GNR films are an interlinked network, but the ribbons and pores are uniformly distributed and lack thick regions. This, combined with ultrathin film dimensions while also possessing significant optical transparency, support excellent RF transparency that is consistent with theoretical values up to very high power density. Production of RF-transparent films that are also optically transparent while still being useful for deicing would extend applications to automotive glass and specialized window coating materials.^{13,14}

Here we report HD-GNR thin films that are highly RF-transparent, namely, up to a RF power density of $\sim 2 \times 10^5 \text{ W/m}^2$ as permitted by the thermal capability of the underlying glass substrate. The HD-GNR films are also optically transparent enough for many tinted glass or plastics applications. Both the RF and optical transmittances vary with the sheet resistance of the HD-GNR films, which can be tuned based on the film thickness. We expand a model based on skin depth theory to explain the RF transmission through the HD-GNR films. The skin depth (or decay length) of the RF wave in HD-GNR films is hundreds of microns, allowing RF-transparency of sub-skin depth films. The quality and uniformity of the films is a contributing factor to the high RF-transparency due to mitigation of thick HD-GNR regions or spots on the films. A voltage-induced deicing is also demonstrated.

Experimental Methods

HD-GNR synthesis and film preparation

CAUTION: Na/K is a potent reductant and is highly reactive. All procedures involving Na/K alloy must be executed with extreme caution. The Na/K and the reaction mixture were prepared in a nitrogen-filled dry box, then sealed with a screw-cap and removed from the dry box, and the mixture was stirred with a magnetic stirrer in the hood. Piranha (used to clean the glass substrates) is a strong oxidant and must also be handled with care. Personal protective equipment including thick rubber gloves, flame-retardant lab coat, goggles and face shield should be worn at all times during the experiment.

Organic-soluble HD-GNRs were synthesized by splitting multiwalled carbon nanotubes (MWCNTs) using Na/K alloy in 1,2-dimethoxyethane and alkylating the edges with 1-iodohexadecane (Figure 1a).¹⁵⁻¹⁷ Upon completion of the reaction, the Na/K alloy was *slowly and carefully* quenched with methanol and the product was washed sequentially with methanol, water, and diethyl ether. The sample was dried *in vacuo* for 24 h. (These HD-GNRs are now available commercially through AZ Electronic Materials Corp. and Sigma-Aldrich). The HD-GNRs were then suspended in *ortho*-dichlorobenzene (ODCB) at a concentration of 0.5 mg/mL and bath-sonicated for 15 min (12 W model 08849-00, Cole-Parmer) before use. The concentration of the HD-GNR solution was found to be optimal for spray-coating. Low concentrations required prolonged spraying to achieve the required film density. Concentrations that were too high made it difficult to finely control the film thickness to remain optically transparent. Non-functionalized GNR stacks were difficult to disperse in solvents¹⁵ to form a stable dispersion for spray-coating films without thick spots. Functionalization with hexadecyl groups enabled dispersion in organic solvents, such as *ortho*-dichlorobenzene, as reported in our earlier work on HD-GNR synthesis where detailed solubility studies can be found.¹⁵ Microscope soda lime glass slides (McMaster, 1 mm thick) were cleaned with piranha (7:4 v/v solution of H₂SO₄ and 35% H₂O₂), rinsed with copious amounts of de-ionized water and blow-dried with a nitrogen stream. With an Iwata airbrush connected to compressed nitrogen, the HD-GNR solution was spray-coated on the glass slide that had been placed on a hot plate heated to 200 °C. At this temperature, the HD-GNRs formed a uniform film on the glass with rapid evaporation of the solvent. After cooling to room temperature, polyurethane (clear-coat Dupli-Color™ auto paint, O'Reilly Auto Parts) was spray-coated over the HD-GNRs to provide a robust film. Since the HD-GNRs form a porous network on the glass, there is sufficient glass exposure for the adhesion of the polyurethane to the glass surface.

Characterization

SEM images were acquired on a JEOL 6500 SEM. Raman spectra of powdered samples placed on a glass slides were acquired using Renishaw inVia Raman microscope equipped with 514 nm Ar ion laser. X-ray diffractograms were obtained on a Rigaku D/Max Ultima II Powder XRD with Cu K α (λ = 1.5418 Å) diffractometer using a zero background holder. Optical transmittance was obtained using a Shimadzu UV-3101PC UV-vis-NIR spectrophotometer. In order to determine the sheet resistance, the film resistance was measured using a two-terminal method

with a Cen-Tech digital multimeter. This was further shown to be equivalent to four-terminal measurements (Figure S1). To eliminate contact resistance between the probes and the film, silver electrodes were deposited by applying colloidal silver paste (Pelco Colloidal Silver Liquid, Ted Pella) on both ends of a 7.62 cm \times 2.54 cm film; they were used for contact to the probes. Sheet resistance, R_s , was thus calculated based on the measured resistance and film geometry with $R_s = \text{measured resistance} \times w/l$ where w and l are the width and length of the film, respectively. The DC conductivity, σ_0 , was calculated with $\sigma_0 = \frac{1}{R_s \times d}$ where d is the film thickness.

Results and Discussion

The HD-GNR films consist of an isotropic array of HD-GNRs (Figure 1a). The films studied vary from 50 nm to 200 nm thickness. Individual HD-GNRs are, on average, a 30 nm thick multilayer stack of HD-GNR layers.¹⁵ They are 1 to 50 μ m long (average \sim 10 μ m) and 50 to 350 nm wide (average \sim 250 nm) (Figure 1b, c). Based on microscopic studies, the outer tubes are clearly split but whether the innermost tubes are split (Figure 1c) is uncertain. Based on the X-ray diffractogram in Figure 1d, the (002) peak of the HD-GNRs at 25.8° is close to that exhibited by a graphitic structure (26.3°) but with additional distinctive features. The pronounced asymmetry and shoulder of the (002) peak, coupled with the (001) peak at 12° is characteristic of intercalation with hexadecyl groups.¹⁵ During the synthetic step at which the MWCNTs were treated with 1-iodohexadecane for edge functionalization, a significant amount of the moieties intercalated into the tube layers that were not split.¹⁵

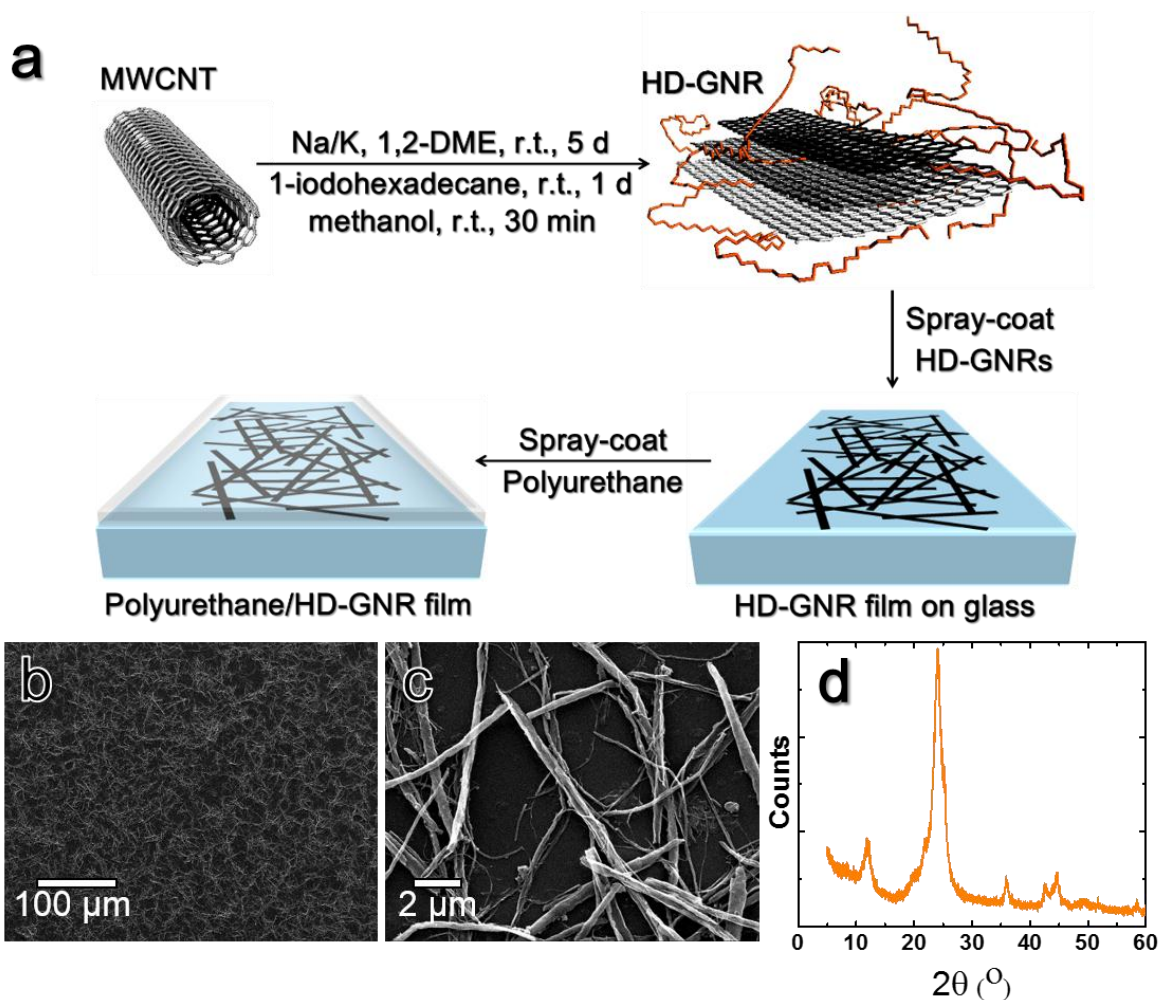


Figure 1. Fabrication and characterization of the HD-GNR film before coating with polyurethane. a) Schematic of the HD-GNR synthesis and film fabrication. b) SEM image of the HD-GNR film morphology. c) SEM image of the HD-GNR film that shows HD-GNRs connected to form a percolating network. d) X-ray diffractogram of the HD-GNR film. e) Raman spectrum of the HD-GNR film.

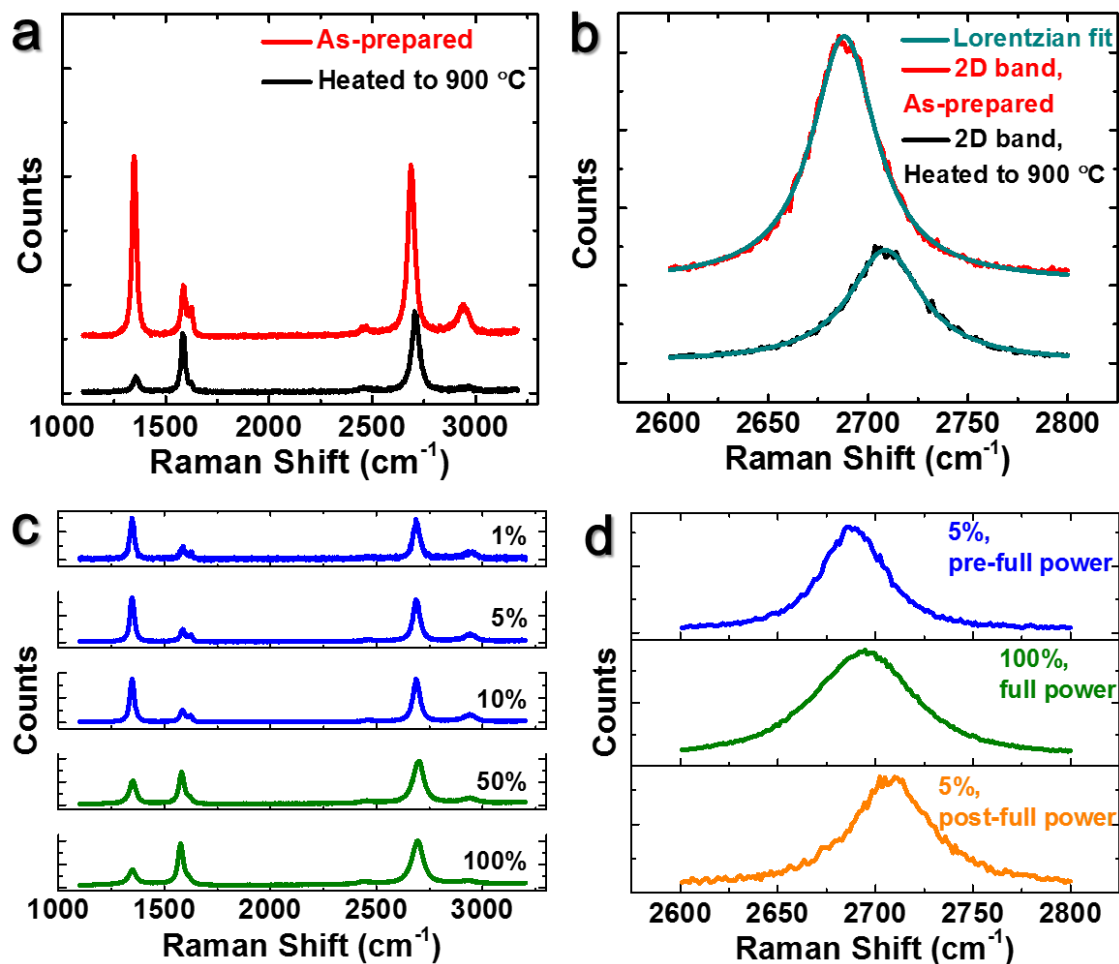


Figure 2. Raman spectroscopy of HD-GNRs. a) Raman spectra of HD-GNRs–as-prepared (red), heated to 900 °C (black). b) 2D bands of HD-GNRs–as-prepared (red), heated to 900 °C (black). Lorentzian fits of the 2D bands (cyan). c) Excitation laser power effect on Raman spectrum of HD-GNRs. Spectra were collected from the same spot of the HD-GNR powder sample in the order presented in the plot. 100% power = 25 mW. d) 2D bands of HD-GNR before and after measurement at 100% laser power.

Raman spectroscopy is a well-established technique for studying the stacking of graphene.¹⁸⁻²² A multilayer graphene stack is not inevitably AB-stacked or graphitic.^{19,23} Spectroscopic measurements are used here to determine the stacking order, or lack thereof, of the multilayer HD-GNRs. The strong characteristic Raman G and 2D bands at $\sim 1587 \text{ cm}^{-1}$ and $\sim 2688 \text{ cm}^{-1}$, respectively, indicate that the HD-GNRs maintain the basal plane π -conjugated sp^2 -carbon structure.^{15,16,19,24} Though the HD-GNRs are not monolayer, their Raman spectra exhibit

features of monolayer graphene films. The Raman spectrum shows an I_G/I_{2D} ratio of 0.29 (Figure 2a), a single Lorentzian 2D band and a 2D bandwidth of 40 cm^{-1} (Figure 2b). It is well-documented that monolayer graphene features an I_G/I_{2D} ratio of ≤ 0.50 , a single Lorentzian 2D, a bandwidth of $\leq 33\text{ cm}^{-1}$ and a 2D band position at 2680 cm^{-1} .^{18-22,25,26} The $I_G/I_{2D} \leq 0.50$,

upshifted 2D band position, and larger but single Lorentzian 2D bandwidth observed for the HD-GNRs compared to those for monolayer graphene have also been reported for non-oriented or non-AB-stacked multilayer graphene formed as-grown²³ or by folding^{27,28} or *ex situ* stacking¹⁸ of monolayer graphene films. The I_G/I_{2D} and lineshape for monolayer graphene, non-AB-stacked graphene and HD-GNRs are thus similar. These Raman features for multilayer graphene and HD-GNRs are due to non-graphitic stacking that exhibits weaker interlayer electronic interactions than the AB-stacked graphite.^{19,26,29} In contrast, AB-stacked graphite spectrum consists of a more intense G band, a strongly upshifted 2D band that has a larger bandwidth ($> 60\text{ cm}^{-1}$) and that can be fitted with two Lorentzians.^{19,26,30} As such, AB-stacked GNRs with 2 to 40 layers²⁴ were reported to feature Raman characteristics similar to those of graphite. The non-AB-stacked GNRs reported here can be called turbostratic graphene nanoribbons, multilayer graphene nanoribbons, graphene nanoribbon stacks, or simply, graphene nanoribbons.

The relative intensity of the D band with respect to the G band of HD-GNRs (I_D/I_G ratio ~ 3.7) is higher than that of defunctionalized HD-GNRs (I_D/I_G ratio ~ 0.23) (Figure 2a). The higher I_D/I_G ratio is attributed to the MWCNT splitting, hexadecylated edges, and intercalation of the HD-GNRs.¹⁵ It should be noted that HD-GNRs, due to their relatively higher edge content, always show a larger D band^{15,16} than their large graphene flake^{18,25,31} or unfunctionalized GNR counterparts.^{16,24} After heating the HD-GNRs to $900\text{ }^\circ\text{C}$ under Ar at $20\text{ }^\circ\text{C/min}$, the I_D/I_G ratio is significantly reduced because of defunctionalization (Figure 2a).¹⁵ Though edge-functionalized and intercalated edges are removed,¹⁵ the non-AB stacking of the GNRs is retained as shown by Raman 2D band characteristics (Figure 2b).

During Raman measurements, a sufficiently low excitation laser power is critical in preserving the intrinsic Raman features.²⁶ Changes in the Raman spectral features of HD-GNRs could appear in the form of a change in I_D/I_G ³² or shifts of the Raman bands³²⁻³⁵ due to laser-induced temperature effects. Laser powers of 2.5 mW or lower do not induce changes in the spectral features (Figure 2c). However, Raman spectra obtained with laser power of 12.5 mW or higher show smaller I_D/I_G ratios (Figure 2c) that arise from defunctionalization due to the laser-induced temperature increase. Thus, the Raman spectra obtained at higher power alter the sample through defunctionalization, and the increase in temperature affects the analyses. Subsequent low power Raman analysis of the laser-heated sample shows that the 2D band is more upshifted than apparent during the relatively high power Raman measurement (Figure 2d). This result of low power measurement after laser-induced heating is consistent with the Raman spectrum of the thermally heated sample in Figure 2a.

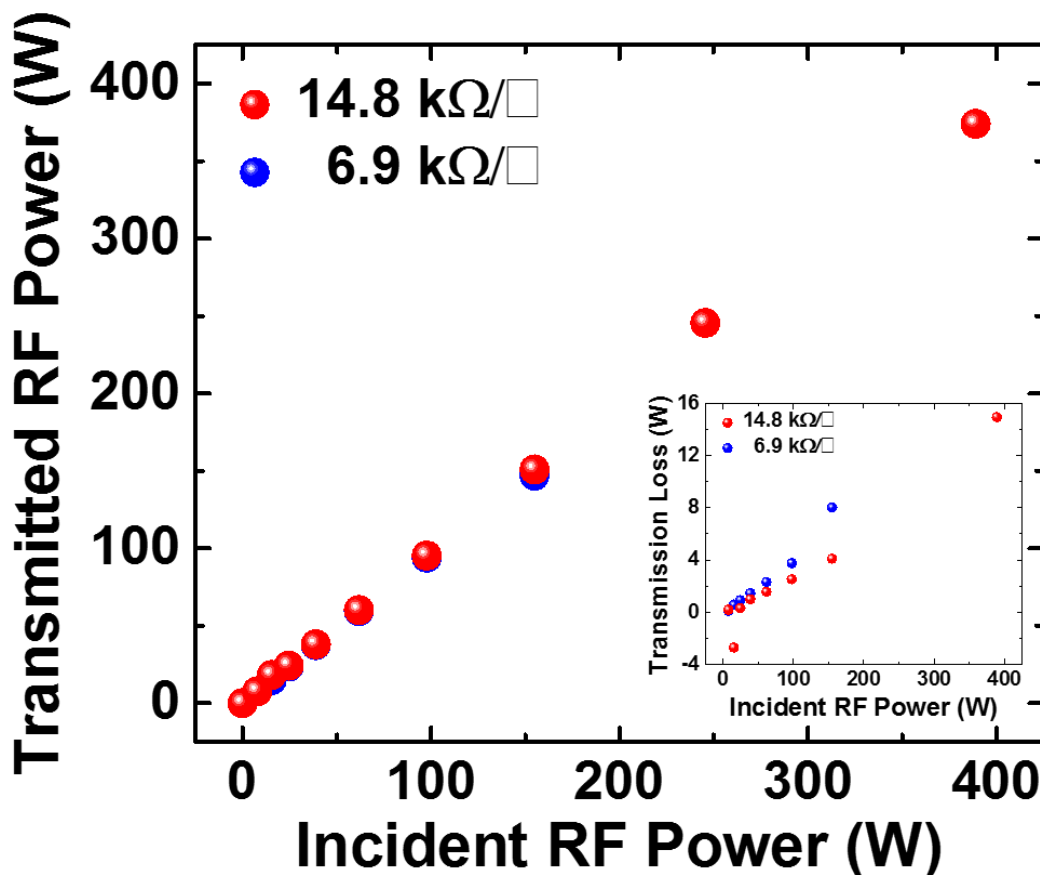


Figure 3. Transmitted vs incident RF power for two different films, designated with red and blue dots, sprayed to different thicknesses that had the designated sheet resistances of 14.8 kΩ/□ and 6.9 kΩ/□, respectively. Resistances were measured with a two point probe with silver electrodes at both ends of the film and sheet resistance was calculated based on the film geometry (Experimental Methods and Figure S1). The transmitted powers are of the HD-GNR films only and those of the protective polyurethane coatings were subtracted. Inset: Transmission loss vs. incident RF power.

Figure 3 shows the RF transmission measurements through HD-GNR films. For the highly uniform films produced in separate experiments on a glass substrate with sufficient thermal conductivity, the transmitted power increases linearly with the incident power. The RF transmittance was ~ 99% and ~ 98% for the two films of ~ 85 nm and ~ 110 nm thickness, respectively, and designated with red and blue dots, respectively, in Figure 2. Thus, there is a very small percentage of power loss during transmission up to 390 W (2×10^5 W/m²) as permitted by the thermal capability of the substrate (Figure 3 inset). The linear relationship

(slope = 1) between incident and transmitted RF indicates that the HD-GNR films are homogenous, consistent with the SEM images. According to our previous work,¹ the transmitted power becomes non-linear as the incident power increases for the reported non-homogenous film. The transmitted power approached a plateau after 20 W (7×10^3 W/m²) and subsequently dropped as the heating melted the polyurethane coating and further carbonized the polyurethane-coated polyimide substrate. This was attributed to the electromagnetic and the resulting thermal energy concentration in the thick regions generated by non-uniform dispersion of the HD-GNR films where HD-GNRs were spray-coated at 200 °C atop polyurethane pre-coated on polyimide; the resulting coating was black and optically opaque. During the deposition, the nanoscale-thick polyurethane would be in a gel-like state and the underlying micron-scale-thick polyimide would buckle, yielding a non-uniform film with some thick regions. In the present work, however, the HD-GNR films were first deposited on a glass surface and polyurethane was deposited atop as a protection layer. Thus, the HD-GNR films formed a homogenous percolating network on the glass without thick regions. Any GNR-thick regions would have been optically black, further resulting in significant RF absorbance since they are > 250 nm thick. The fabrication of the uniform dispersion was done by monitoring the visual optical transparency and ensuring the absence of black, thicker locations. Optical transmittance measurements (discussed later) obtained at several locations on the film after

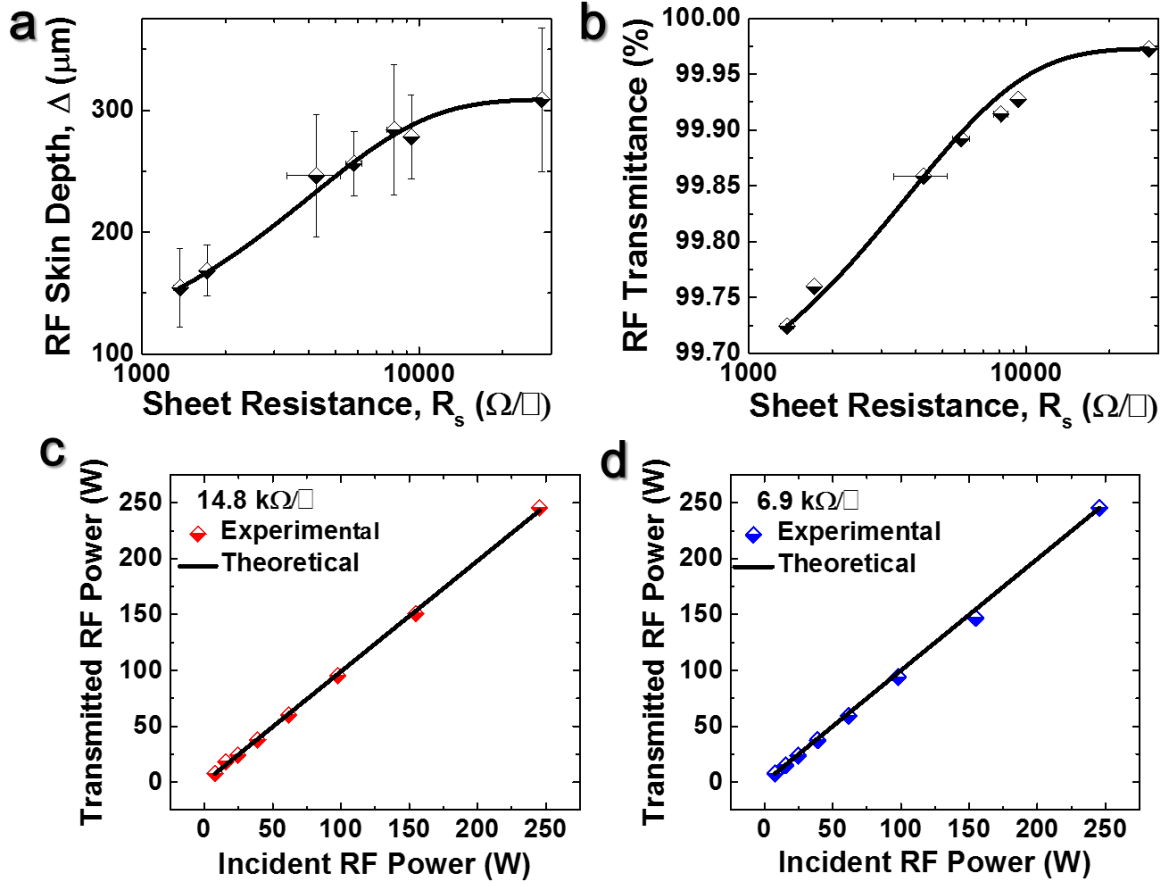


Figure 4. Predictions from electromagnetic skin depth theory. a) Dependence of the theoretical RF skin depth on the sheet resistance of the HD-GNR film. b) Dependence of the calculated RF transmittance on the sheet resistance of the HD-GNR. c) Transmitted RF power (experimental and theoretical) vs. incident RF power for a HD-GNR film with a resistance of 14.8 $\text{k}\Omega/\square$. d) Transmitted RF power (experimental and theoretical) vs. incident RF power for a HD-GNR film with a resistance of 6.9 $\text{k}\Omega/\square$.

fabrication were reproducible to $\pm 2\%$ (standard deviation), verifying the visual observation of uniformity. This uniformity proves to be essential for the desired RF transparency without the thicker regions that can significantly increase absorption at higher RF powers.

In describing wave propagation through the conductive HD-GNR film, the electric field component \vec{E} (in V/m) of a uniform plane wave traveling in a given direction, z , perpendicular to the surface of the film, is given as eq 1.³⁶

$$\tilde{\mathbf{E}}(z, t) = \tilde{\mathbf{E}}_0 e^{i(\tilde{k}z - \omega t)} \quad (1)$$

where $\tilde{\mathbf{E}}_0$ (in V/m) is the electric field vector parallel to the film surface and “ \tilde{k} ” (in 1/m) is the complex wave number such that eq 2 applies:

$$\tilde{k} = k + i\kappa \quad (2)$$

$\tilde{\mathbf{E}}$ is expressed in terms of the real and the imaginary parts of \tilde{k} as in eq 3:

$$\tilde{\mathbf{E}}(z, t) = \tilde{\mathbf{E}}_0 e^{-\kappa z} e^{i(kz - \omega t)} \quad (3)$$

The imaginary part shows exponential attenuation of the amplitude $\tilde{\mathbf{E}}_0$ with respect to the distance z from the surface of the material. As a result, the distance through the material in which the field diminishes to $1/e$ or $\sim 37\%$ of its value from the surface satisfies eq 4:

$$\kappa z = 1 \quad \text{or} \quad z = 1/\kappa \quad (4)$$

This distance is referred to as the skin depth and will be denoted by Δ (in m) and eq 5 applies:

$$\Delta = \frac{1}{\kappa} = \frac{1}{\sqrt{\pi \sigma \mu_0 f}} \quad (5)$$

where σ is the material conductivity at frequency f , μ_0 is the permeability of free space, all in the S.I. units. The skin depth characterizes the depth of electromagnetic wave propagation into a typical conductor. Since $e^2 \approx 10$, the electromagnetic wave loses 90% of its energy on its path at every skin depth. The application of this concept to describe RF transmission in HD-GNR thin films was previously suggested and proven through waveguide RF measurements at frequencies

between 2 and 4 GHz.¹ It was demonstrated that, similar to classical conductors, the RF conductivity was very close to the DC conductivity of HD-GNR thin films.

When a traveling free-space plane-wave is incident on the front boundary of an HD-GNR film, a portion of the wave energy is reflected from the film back to free space while the propagation continues inside the HD-GNR film.^{36,37} As this propagated wave reaches the back boundary, it is reflected again in the direction of the front boundary with the phase shift $\varphi = kz$; and the remaining energy is transmitted to the free space behind the HD-GNR film.

Therefore, the total reflected wave from the front boundary and transmitted wave through the film are superpositions of multiple partial waves moving back and forth. The total transmission loss is the sum of reflection/mismatch loss and HD-GNR absorption loss of the wave defined by eq 3. But the thickness of the HD-GNR film is such a small fraction of the wavelength that all the reflected waves at the front boundary are in almost opposite phase and cancel each other. In addition, since mismatch loss, from waveguide measurements, does not exceed 1% of incident power,¹ the main part of the loss is the HD-GNR absorption loss defined by the skin depth (eq 5) that increases at higher sheet resistance (Figure 4a) due to lower conductivity at higher sheet resistance (eq 5, Table S1). Thus, the RF transmittance for a film is related to its skin depth Δ

and thickness d by eq 6:³⁷

$$T = P_T / P_0 = (E_{0,T} / E_{0,I})^2 = e^{-2d/\Delta} \quad (6)$$

where P_T and P_0 (in W) are transmitted and incident RF powers and $E_{0,T}$ and $E_{0,I}$ (in V/m) are transmitted and incident amplitudes, respectively, through the HD-GNR film. As with the skin depth, the RF transmittance increases with higher sheet resistance (Figure 4b). In order to validate this theory for HD-GNR films, the transmitted RF powers were compared with a series of incident RF powers for the two films measured in Figure 3. The results demonstrate an excellent match between the theoretical calculations and the experimental measurements (Figures 4c, d) for the sample HD-GNR films, thus supporting the classical conductivity behavior at radio frequencies. Thus, for a thin HD-GNR film, the wave propagates with an amplitude very close to that of the incident wave. As a result, the HD-GNR film is transparent to the RF wave.

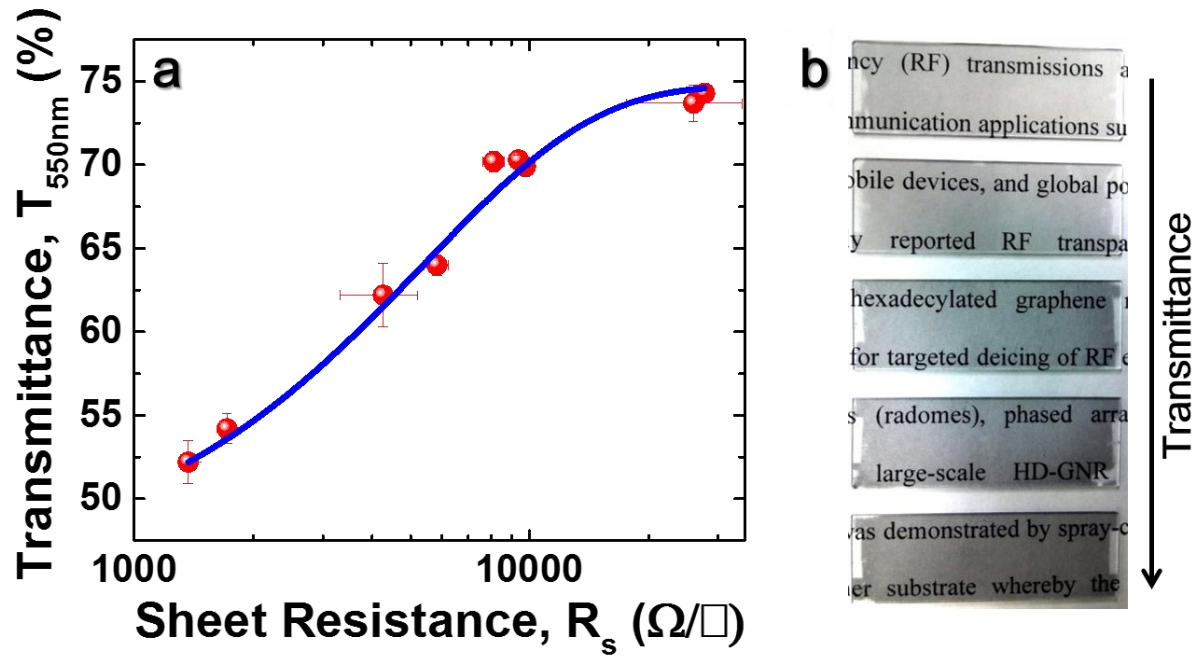


Figure 5. a) Optical transmittance dependence on sheet resistance of HD-GNR films. The sheet resistances were measured as described in the Experimental Methods above using the two-terminal measurement technique (see Figure S1 for comparison to four-terminal measurements). Transmittance of HD-GNR films at 550 nm vs sheet resistance. The resistances are of the HD-GNR films without polyurethane coating. b) Photograph showing optical transparency through the HD-GNR films with transmittance from 75% (top) to 50% (bottom).

Sheet resistances and optical transmittances of the HD-GNR films can also be tuned by varying the film thicknesses. In Figure 5a, the optical transmittance of the films increase with increasing sheet resistance. Images in Figure 5b show the decreasing optical transmittance of HD-GNR films from 75% to 50%. At $> 65\%$ optical transmittance, the sheet resistance of the HD-GNR film is $\sim 6 \text{ k}\Omega/\square$. With this amount of resistance, the film is suitable as a thin film resistor where heating power $P = V^2/R$ can be delivered through the film subject to an applied

voltage.

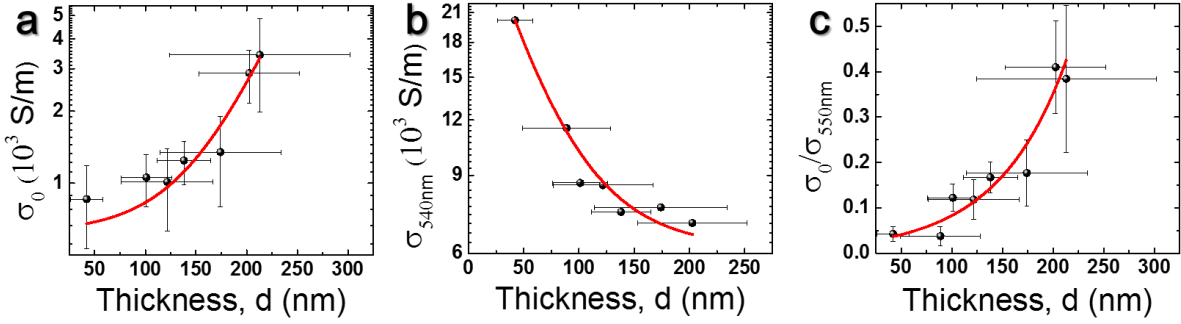


Figure 6. DC and optical conductivity of HD-GNR films. a) DC conductivity of HD-GNR films as a function of thickness. b) Optical conductivity of HD-GNR films as a function of thickness. c) DC conductivity/optical conductivity ratio of HD-GNR films as a function of thickness. The conductivities and thicknesses are of the HD-GNR films without polyurethane coating.

Though optical transparency is not essential in many applications of RF transparent conductive HD-GNR films, certain applications would require optical transparency in addition to RF transparency. The transmission properties of HD-GNR films in the visible region can be evaluated by studying the relationship between DC (*i.e.* zero frequency) and optical (*i.e.* frequency-dependent) conductivities. The DC conductivity ($\sigma_0 = \frac{1}{R_s \times d}$, Experimental Methods) of HD-GNR films is found to increase with the thickness (Figure 6a). The sheet resistance of a material depends on the thickness. However, the electrical conductivity of a uniform, homogenous material is thickness-independent provided that the uniformity is invariant with thickness. Thus, increase in the DC conductivity is due to increase in the film density rather than the film thickness. This behavior is similar to that observed for carbon nanotube^{38,39} and silver nanowire films.⁴⁰ Unlike those films, however, the optical conductivity, σ_{550nm} , of HD-GNR films decreases with the film thickness (Figure 6b), producing optical conductivity/DC conductivity ratio greater than unity ($\frac{\sigma_{550nm}}{\sigma_0} > 1$) (Figure 6c). This behavior is similar to that observed in chemically exfoliated graphene films.⁴¹ Thus, the sheet resistance of the HD-GNR films is required to be high in order for the second term in eq 7, below, to approach zero so as to produce an optical transmittance that approaches unity or 100%:³⁸⁻⁴⁰

$$T = (1 + \frac{188\sigma_{550nm}}{R_s\sigma_0})^{-2} \quad (7)$$

Film density is an important parameter for obtaining a low $\frac{\sigma_{550nm}}{\sigma_0}$; however, the thickness and width of individual components of the film has to be small as well in order to reduce the

overall film thickness. Carbon nanotube films and silver nanowire films were reported to exhibit $\frac{\sigma_{550\text{nm}}}{\sigma_0} < 1$. The thickness of an individual carbon nanotube³⁹ was 2.4 nm and an individual

silver nanowire⁴⁰ was 85 nm. This enabled fabrication of sub-100-nm-thick, dense films with high optical transmittance and low sheet resistance.³⁸⁻⁴⁰ The foliated HD-GNRs (in stacks) reported here are ~ 30-nm-thick and ~ 250 nm wide, and the films made from them are 50 to 200 nm thick. Since the optical conductivity/DC conductivity ratio of HD-GNR films decreases with higher film density thick (Figure 6c), our results suggest that if the individual HD-GNRs were of much smaller width and thickness, the film density could be significantly increased but with film thicknesses being much lower than those obtained here.⁴² Thus, HD-GNR films with lower optical conductivity relative to the DC conductivity may be obtained, i.e. $\frac{\sigma_{550\text{nm}}}{\sigma_0} < 1$; a condition

that would facilitate fabrication of HD-GNR films with high optical transmittance at low sheet resistance. However, efficient exfoliation of the GNRs derived from MWCNTs has been, hitherto, unattainable.¹⁵⁻¹⁷

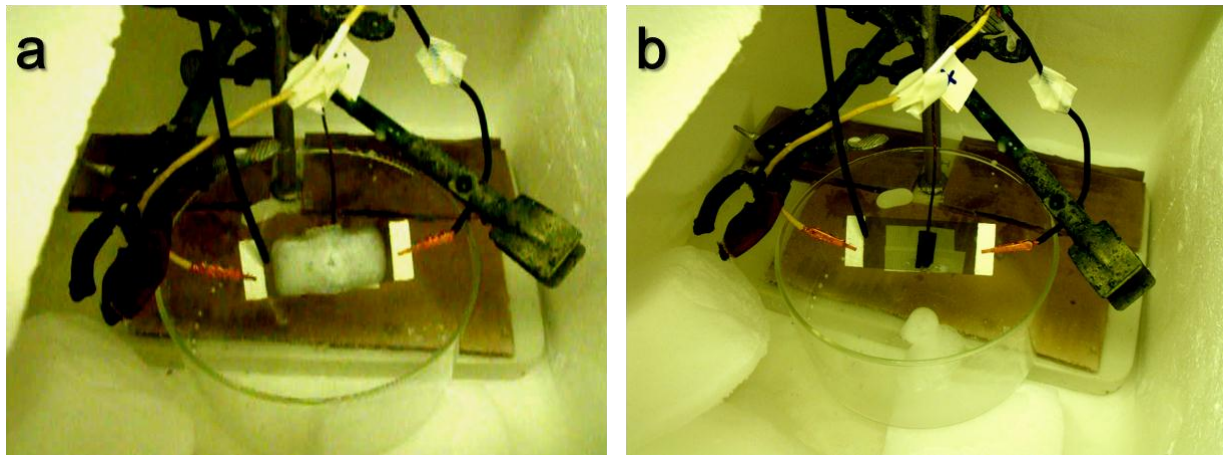


Figure 7. Photographs of resistively heated HD-GNR films at - 20 °C. a) During deicing. b) After deicing which took 3.7 min. The experiment was conducted in a Styrofoam box maintained at - 20 °C. The sample was mounted at an angle of ~ 40° so that the partially melted ice could slide off. The ice that melted off the surface can be seen rapidly refreezing once it hits the dish below. A surface thermocouple was taped to the bottom of the polyurethane-HD-GNR-coated glass slide. All heating was done through an applied voltage to the left and right ends of the film. The HD-GNR film has a resistance of 3.3 kΩ, a thickness of 140 nm and an optical transmittance (at 550 nm) of 70%.

In order to demonstrate deicing capability with the HD-GNR films, an HD-GNR film with a resistance of 3.8 k Ω was fabricated on a glass slide and mounted in a Styrofoam box cooled to - 20 °C (Figure 7a). A voltage of 190 V was applied across the film through silver contacts on both ends providing $\sim 1.3 \text{ W/cm}^2$ to the film. The ice melted and then detached entirely in 3.7 min (Figure 7b), underscoring the deicing capability along with the RF and optical transparency discussed above.

Conclusion

In summary, we have demonstrated that conductive HD-GNR thin films can be produced with high uniformity. We verified 99% RF transmission at a power density up to $2 \times 10^5 \text{ W/m}^2$ in an 85 nm thick HD-GNR film with an optical transmittance of 75%. The small HD-GNR film thickness relative to the large skin depth and propagation wavelength through the film permits the exceedingly high RF transmission at high RF power. The absence of thick spots and relatively high thermal conductivity of the substrate is crucial to transparency at high RF power. We also demonstrated the possibility of obtaining more optically transparent films with better exfoliated HD-GNRs. The optical transparency is important in controlling the quality of fabricated RF transparent films as optical transmittance could be easily measured at different regions of the film to assess uniformity and the presence of thick spots. Finally, the RF and optically transparent films permitted voltage-induced deicing.

References

1. Volman, V.; Zhu, Y.; Raji, A.-R. O.; Genorio, B.; Lu, W.; Xiang, C.; Kittrell, C.; Tour, J. M. Radio-Frequency-Transparent, Electrically Conductive Graphene Nanoribbon Thin Films as Deicing Heating Layers. *ACS Appl. Mater. Interfaces* **2014**, *6*, 298-304.
2. Zhang, P.; Lau, Y. Y.; Gilgenbach, R. M. Analysis of Radio-frequency Absorption and Electric and Magnetic Field Enhancements due to Surface Roughness. *J. Appl. Phys.* **2009**, *105*, 114908.
3. Bosman, H.; Lau, Y. Y.; Gilgenbach, R. M. Microwave Absorption on a Thin Film. *Appl. Phys. Lett.* **2003**, *82*, 1353-1355.
4. Bosman, H.; Lau, Y. Y.; Gilgenbach, R. M. Power Absorption by Thin Films on Microwave Windows. *IEEE Trans. Plasma Sci.* **2004**, *32*, 1292-1297.
5. Dan, B.; Irvin, G. C.; Pasquali, M. Continuous and Scalable Fabrication of Transparent Conducting Carbon Nanotube Films. *ACS Nano* **2009**, *3*, 835-843.
6. Becerril, H. A.; Mao, J.; Liu, Z.; Stoltenberg, R. M.; Bao, Z.; Chen, Y. Evaluation of Solution-Processed Reduced Graphene Oxide Films as Transparent Conductors. *ACS Nano* **2008**, *2*, 463-470.
7. Eda, G.; Lin, Y. Y.; Miller, S.; Chen, C. W.; Su, W. F.; Chhowalla, M. Transparent and Conducting Electrodes for Organic Electronics from Reduced Graphene Oxide. *Appl. Phys. Lett.* **2008**, *92*, 233305.

8. Zhu, Y. W.; Cai, W. W.; Piner, R. D.; Velamakanni, A.; Ruoff, R. S. Transparent Self-Assembled Films of Reduced Graphene Oxide Platelets. *Appl. Phys. Lett.* **2009**, *95*, 103104.
9. Li, Y.; Chen, Z.; Zhang, S.; Ni, Y.; Huang, J. Electrical Conductivity and Electromagnetic Interference Shielding Characteristics of Multiwalled Carbon Nanotube Filled Polyacrylate Composite Films. *Appl. Surf. Sci.* **2008**, *254*, 5766–5771.
10. Song, W.-L.; Cao, M. S.; Lu, M.-M.; Bi, S.; Wang, C. Y.; Liu, J.; Yuan, J.; Fan, L.-Z. Flexible Graphene/Polymer Composite Films in Sandwich Structures for Effective Electromagnetic Interference Shielding. *Carbon* **2014**, *66*, 67-76.
11. Hu, M.; Gao, J.; Dong, Y.; Li, K.; Shan, G.; Yang, S.; Li, R. K.-Y. Flexible Transparent PES/Silver Nanowires/PET Sandwich-Structured Film for High-Efficiency Electromagnetic Interference Shielding. *Langmuir* **2012**, *28*, 7101–7106.
12. Yu, Y. H.; Ma, C.-C. M.; Teng, C.-C.; Huang, Y.-L.; Lee, S.-H.; Wang, I.; Wei, M.-H. Electrical, Morphological, and Electromagnetic Interference Shielding Properties of Silver Nanowires and Nanoparticles Conductive Composites. *Mater. Chem. Phys.* **2012**, *136*, 334-340.
13. Stolhofer, D.; Doecke, H.; Liu, Y.; O'earry, P. RF Propagation Through Transparent Conductors in Energy Efficient Windows. Proceedings of the 16th European Wireless Conference, Lucca, Italy, April 12-15, 2010; IEEE: Piscataway, NJ, 2010.
14. Granqvist, C. G. Transparent Conductors as Solar Energy Materials: A Panoramic Review. *Sol. Energ. Mat. Sol. Cells* **2007**, *91*, 1529-1598.
15. Genorio, B.; Lu, W.; Dimiev, A. M.; Zhu, Y.; Raji, A.-R. O.; Novosel, B.; Alemany, L. B.; Tour, J. M. *In Situ* Intercalation Replacement and Selective Functionalization of Graphene Nanoribbon Stacks. *ACS Nano* **2012**, *6* 4231-4240.
16. Kosynkin, D. V.; Lu, W.; Sinitskii, A.; Pera, G.; Sun, Z.; Tour, J. M. Highly Conductive Graphene Nanoribbons by Longitudinal Splitting of Carbon Nanotubes Using Potassium Vapor. *ACS Nano* **2011**, *5*, 968-974.
17. Lu, W.; Ruan, G.; Genorio, G.; Zhu, Y.; Novosel, B.; Peng, G.; Tour, J. M. Functionalized Graphene Nanoribbons via Anionic Polymerization Initiated by Alkali Metal-Intercalated Carbon Nanotubes. *ACS Nano* **2013**, *7*, 2669-2675.
18. Sun, Z.; Raji, A.-R. O.; Zhu, Y.; Xiang, C.; Yang, C.; Kittrell, C.; Samuel, E. L.; Tour, J. M. Large-Area Bernal-Stacked Bi-, Tri-, and Tetralayer Graphene. *ACS Nano* **2012**, *6*, 9790-9796.
19. Malard, L. M.; Pimenta, M. A.; Dresselhaus, G.; Dresselhaus, M. S. Raman Spectroscopy in Graphene. *Phys. Rep.* **2009**, *473*, 51-87.
20. Park, J. S.; Reina, A.; Saito, R.; Kong, J.; Dresselhaus, G.; Dresselhaus, M. S. G' Band Raman Spectra of Single, Double and Triple Layer Graphene *Carbon* **2009**, *47*, 1303-1310.
21. Cong, C.; Yu, T.; Sato, K.; Shang, J.; Saito, R.; Dresselhaus, G. F.; Dresselhaus, M. S. Raman Characterization of ABA- and ABC-Stacked Trilayer Graphene. *ACS Nano* **2011**, *5*, 8760-8768.
22. Lui, C. H.; Li, Z.; Chen, Z.; Klimov, P. V.; Brus, L. E.; Heinz, T. F. Imaging Stacking Order in Few-Layer Graphene. *Nano Lett.* **2011**, *11*, 164-169.

23. Reina, A.; Jia, X.; Ho, J.; Nezich, D.; Son, H.; Bulovic, V.; Dresselhaus, M. S.; Kong, J. Large Area, Few-Layer Graphene Films on Arbitrary Substrates by Chemical Vapor Deposition. *Nano Lett.* **2009**, *9*, 30-35.
24. Cano-Márquez, A. G.; Rodríguez-Macías, F. J.; Campos-Delgado, J.; Espinosa-González, C. G.; Tristán-López, F.; Ramírez-González, D.; Cullen, D. A.; Smith, D. J.; Terrones, M.; Vega-Cantú, Y. I. Ex-MWNTs: Graphene Sheets and Ribbons Produced by Lithium Intercalation and Exfoliation of Carbon Nanotubes. *Nano Lett.* **2009**, *9*, 1527–1533.
25. Li, X.; Cai, W.; An, J.; Kim, S.; Nah, J.; Yang, D.; Piner, R.; Velamakanni, A.; Jung, I.; Tutuc, E.; Banerjee, S. K.; Colombo, L.; Ruoff, R. S. Large-Area Synthesis of High-Quality and Uniform Graphene Films on Copper Foils. *Science* **2009**, *324*, 1312-1314.
26. Ferrari, A. C.; Meyer, J. C.; Scardaci, V.; Casiraghi, C.; Lazzeri, M.; Mauri, F.; Piscanec, S.; Jiang, D.; Novoselov, K. S.; Roth, S.; Geim, A. K. Raman Spectrum of Graphene and Graphene Layers. *Phys. Rev. Lett.* **2006**, *97*, 187401.
27. Ni, Z.; Wang, Y.; Yu, T.; Shen, Z. Raman Spectra of Misoriented Bilayer Graphene. *Phys. Rev. B* **2008**, *78*, 113407.
28. Poncharal, P.; Ayari, A.; Michel, T.; Sauvajol, J.-L. Raman Spectroscopy and Imaging of Graphene. *Nano Res.* **2008**, *1*, 273-291.
29. Cançado, L. G.; Takai, K.; Enoki, T.; Endo, M.; Kim, Y. A.; Mizusaki, H.; Speziali, N. L.; Jorio, A.; Pimenta, M. A. Measuring the Degree of Stacking Order in Graphite by Raman Spectroscopy. *Carbon* **2008**, *46*, 272-275.
30. Kaniyoor, A.; Ramaprabhu, S. A Raman Spectroscopic Investigation of Graphite Oxide Derived Graphene. *AIP Advances* **2012**, *2*, 032183.
31. Ferrari, A. C.; Robertson, J. Interpretation of Raman Spectra of Disordered and Amorphous Carbon. *Phys. Rev. B: Condens. Matter Mater. Phys.* **2000**, *61*, 14095–14107.
32. Lim, J. K.; Yoo, B. K.; Yi, W.; Hong, S.; Paik, H.; Chun, K.; Kim, S. K.; Joo, S.-W. Photodetachment of Aryl Moieties from Covalently Functionalized Singlewalled Carbon Nanotubes by UV Laser Irradiation. *J. Mater. Chem.* **2006**, *16*, 2374–2379.
33. Trusovas, R.; Ratautas, K.; Račiukaitis, G.; Barkauskas, J.; Stankevičienė, I.; Niaura, G.; Mažeikienė, R. Reduction of Graphite Oxide to Graphene with Laser Irradiation. *Carbon* **2013**, *52*, 574-582.
34. Calizo, I.; Ghosh, S.; Bao, W.; Miao, F.; Lau, C. N.; Balandin, A. A. Raman Nanometrology of Graphene: Temperature and Substrate Effects. *Solid State Commun.* **2009**, *149*, 1132-1135.
35. Graupner, R. Raman Spectroscopy of Covalently Functionalized Single-wall Carbon Nanotubes. *J. Raman Spectrosc.* **2007**, *38*, 673–683.
36. Griffiths, J. D. *Introduction to Electrodynamics*, 3rd ed.; Prentice Hall: Englewood Cliffs, NJ, 1999.
37. Lipson, A.; Lipson, S. G.; Lipson, H. *Optical Physics*; Cambridge University Press: New York, 2011.
38. De, S.; Lyons, P. E.; Sorel, S.; Doherty, E. M.; King, P. J.; J. Blau, W. J.; Nirmalraj, P. N.; Boland, J. J.; Scardaci, V.; Joimel, J.; Coleman, J. N. Transparent, Flexible, and Highly Conductive Thin Films Based on Polymer-Nanotube Composites. *ACS Nano* **2009**, *3*, 714-720.

39. Mirri, F.; Ma, A. W. K.; Hsu, T.; Behabtu, N.; Eichmann, S. L.; Young, C. C.; Tsentalovich, D. E.; Pasquali, M. High-Performance Carbon Nanotube Transparent Conductive Films by Scalable Dip Coating. *ACS Nano* **2012**, *6*, 9737-9744.
40. De, S.; Higgins, T. M.; Lyons, P. E.; Sorel, S.; Doherty, E. M.; King, P. J.; J. Blau, W. J.; Nirmalraj, P. N.; Blau, W. J.; Boland, J. J.; Coleman, J. N. Silver Nanowire Networks as Flexible, Transparent, Conducting Films: Extremely High DC to Optical Conductivity Ratios. *ACS Nano* **2009**, *3*, 1767-1774.
41. De, S.; King, P. J.; Lotya, M.; O'Neill, A.; Doherty, E. M.; Hernandez, Y.; Duesberg, G. S.; Coleman, J. N. Flexible, Transparent, Conducting Films of Randomly Stacked Graphene from Surfactant-Stabilized, Oxide-Free Graphene Dispersions. *Small* **2010**, *6*, 458-464.
42. Zhu, Y.; Lu, W.; Sun, Z.; Kosynkin, D. V.; Yao, J.; Tour, J. M. High Throughput Preparation of Large Area Transparent Electrodes Using Non-Functionalized Graphene Nanoribbons. *Chem. Mater.* **2011**, *23*, 935-939.

Appendix

Table S1. Properties of HD-GNR films

R_s (k Ω/\square)	27.7	26.0	8.1	5.8	4.3	1.7
d (nm)	42.1	88.8	138.1	174.1	202.6	213.0
σ (S/m)	857.2	432.5	1346.8	550.0	2878.4	3427.9

* R_s is the sheet resistance of the HD-GNR film. d is the thickness of the HD-GNR film. σ is the DC conductivity calculated based on the sheet resistance and the thickness of the HD-GNR film. Conductivity is thickness-independent for a bulk material. However, the density of HD-GNR films is proportional to the thickness; thus, increase in the DC conductivity is related to the increase in film density.

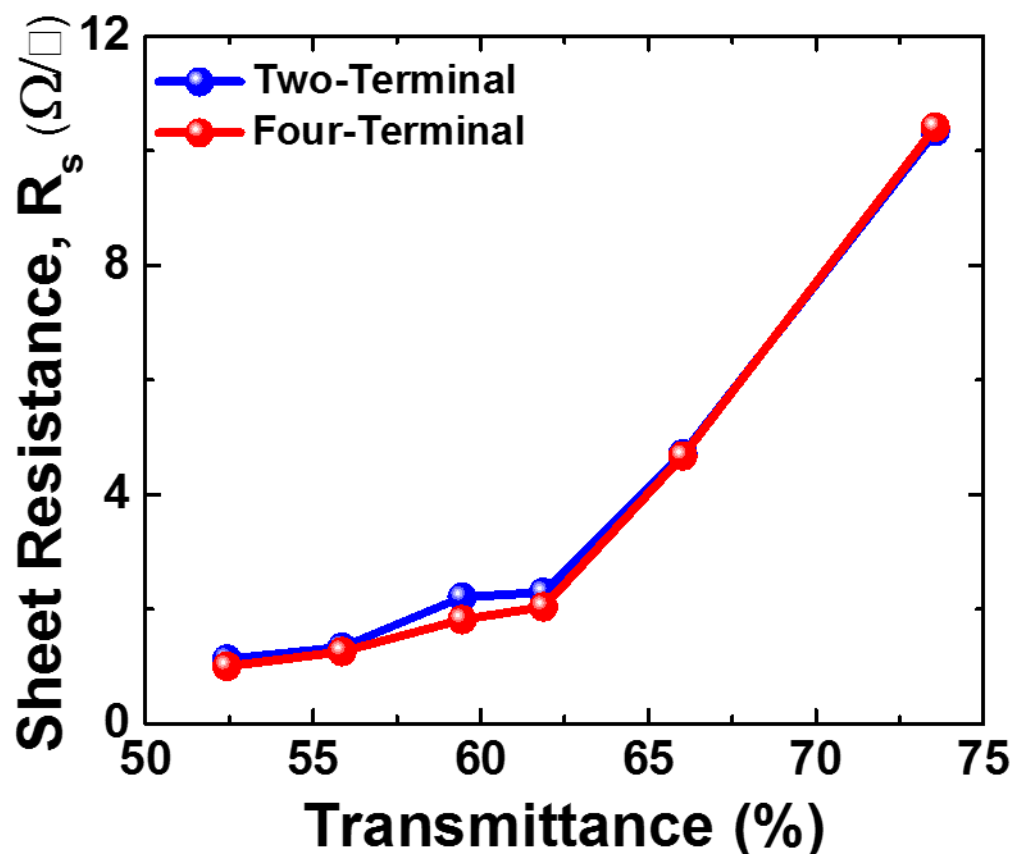
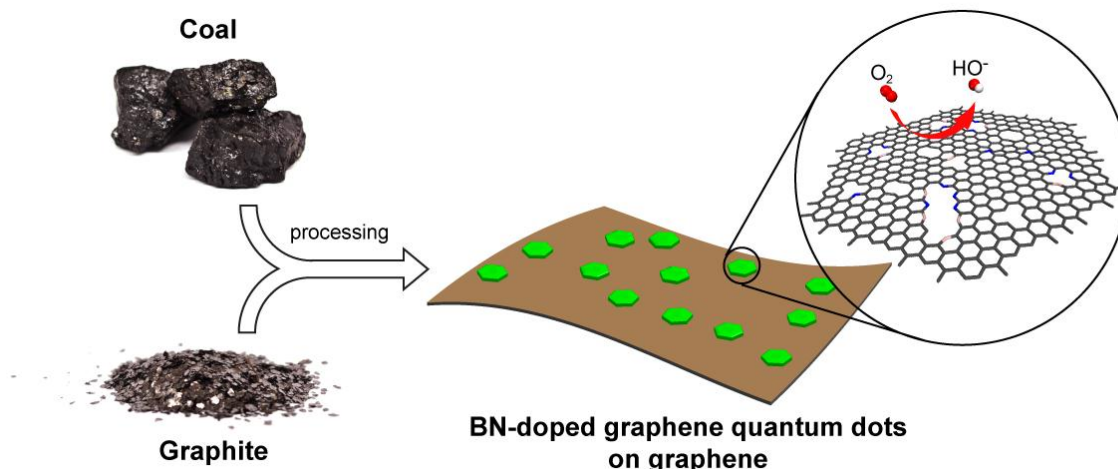


Figure S1. Comparison between the two-terminal and four-terminal measurements. Both methods show excellent agreement with each other. The sheet resistance with the two-terminal measurement is described in the Experimental Methods. The four-terminal measurement was carried out using Alessi four-point probe and Keithley 2010 multimeter. The four-point probe was placed directly on the HD-GNR films without any deposited metal contacts, unlike the two-terminal method. The sheet resistance was determined by $R_s = \frac{\pi V}{\ln 2 I}$. The film size was 7.62 cm \times 2.54 cm, large enough to prevent the need for any correction due to finite size and edge effects that could arise from the four-terminal measurement.

This research summary taken from: Raji, A.-R. O.; Salters, S.; Samuel, E. L. G.; Zhu, Y.; Volman, V.; Tour, J. M. “Functionalized Graphene Nanoribbon Films as a Radiofrequency and Optically Transparent Material,” *ACS Appl. Mater. Interfaces* **2014**, 6, 16661–16668. DOI: <http://dx.doi.org/10.1021/am503478w>

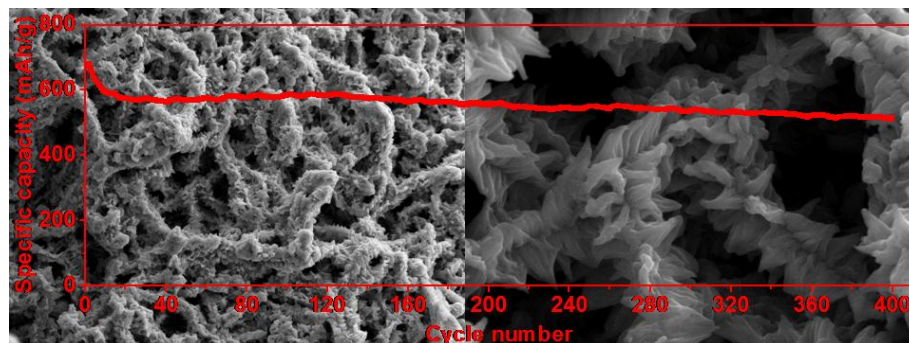
Summaries from Publications of This Reporting Period Supported in Part by the AFOSR



Executive Summary The scarcity and high cost of platinum-based electrocatalysts for the oxygen reduction reaction (ORR) has limited the commercial and scalable use of fuel cells. Heteroatom doped nanocarbon materials have been demonstrated to be efficient alternative catalysts for ORR. Here, graphene quantum dots, synthesized from inexpensive and earth abundant anthracite coal, were self-assembled on graphene by hydrothermal treatment to form hybrid nanoplatelets that were then co-doped with nitrogen and boron by high temperature annealing. This hybrid material combined the advantages of both components, such as abundant edges and doping sites, high electrical conductivity and high surface area, which makes the resulting materials excellent oxygen reduction electrocatalysts with activity even higher than commercial Pt/C in alkaline media.

Fei, H.; Ye, R.; Ye, G.; Gong, Y.; Peng, Z.; Fan, X.; Samuel, E. L. G.; Ajayan, P. M.; Tour, J. M. "Boron- and Nitrogen-Doped Graphene Quantum Dots/Graphene Hybrid Nanoplatelets as Efficient Electrocatalysts for Oxygen Reduction," *ACS Nano* **2014**, *Published on web*. DOI: <http://dx.doi.org/10.1021/nn504637y>

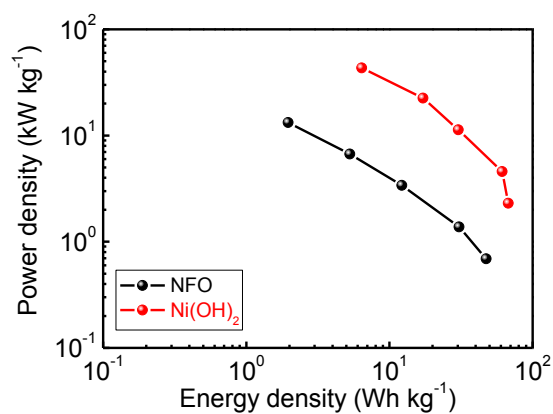
Enhanced Cycling Stability of Lithium Sulfur Batteries Using Sulfur-Polyaniline-Graphene Nanoribbon Composite Cathodes



Executive Summary A hierarchical nanocomposite material of graphene nanoribbons combined with polyaniline and sulfur using an inexpensive, simple method has been developed. The resulting composite, characterized by scanning electron microscopy, transmission electron microscopy, X-ray photoelectron microscopy and X-ray diffraction analysis, has a good rate performance and excellent cycling stability. The synergistic combination of electrically conductive graphene nanoribbons, polyaniline and sulfur produces a composite with high performance. The method developed here is practical for the large-scale development of cathode materials for lithium sulfur batteries.

Li, L.; Ruan, G.; Peng, Z.; Yang, Y.; Fei, H.; Raji, A.-R. O.; Samuel, E. L. G.; Tour, J. M. "Enhanced Cycling Stability of Lithium Sulfur Batteries Using Sulfur-Polyaniline-Graphene Nanoribbon Composite Cathodes," *ACS Appl. Mater. Interfaces* **2014**, 6, 15033-15039. DOI: <http://dx.doi.org/10.1021/am5030116>

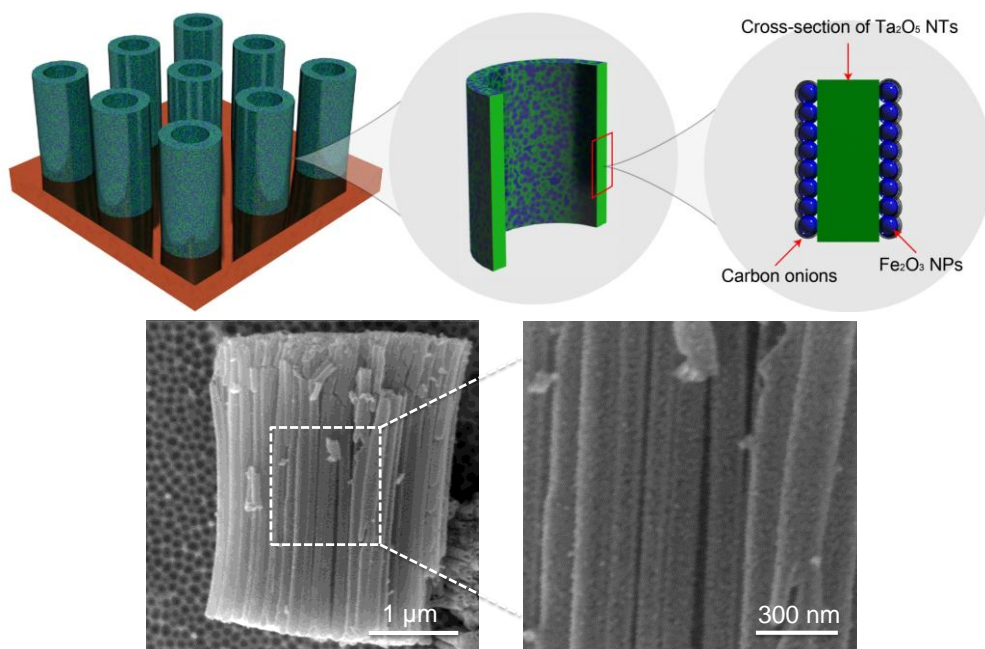
Hydrothermally Formed Three-Dimensional Nanoporous Ni(OH)₂ Thin-Film Supercapacitors



Executive Summary A three-dimensional nanoporous $\text{Ni}(\text{OH})_2$ thin-film was hydrothermally converted from an anodically formed porous layer of nickel fluoride/oxide. The nanoporous $\text{Ni}(\text{OH})_2$ thin-films can be used as additive-free electrodes for energy storage. The nanoporous layer delivers a high capacitance of 1765 F g^{-1} under three electrode testing. After assembly with porous activated carbon in asymmetric supercapacitor configurations, the devices deliver superior supercapacitive performances with capacitances of 192 F g^{-1} , energy densities of 68 Wh kg^{-1} and power density of 44 kW kg^{-1} . The wide working potential window (up to 1.6 V in 6 M aq KOH) and stable cyclability ($\sim 90\%$ capacitance retention over 10000 cycles) make the thin-film ideal for practical supercapacitor devices.

Yang, Y.; Li, L.; Ruan, G.; Fei, H.; Xiang, C.; Fan, X.; Tour, J. M. "Hydrothermally Formed Three-Dimensional Nanoporous $\text{Ni}(\text{OH})_2$ Thin-Film Supercapacitors," *ACS Nano* **2014** 8, 9622–9628. DOI: <http://dx.doi.org/10.1021/nm5040197>

Three-Dimensional Thin-Film for Lithium-Ion Batteries and Supercapacitors

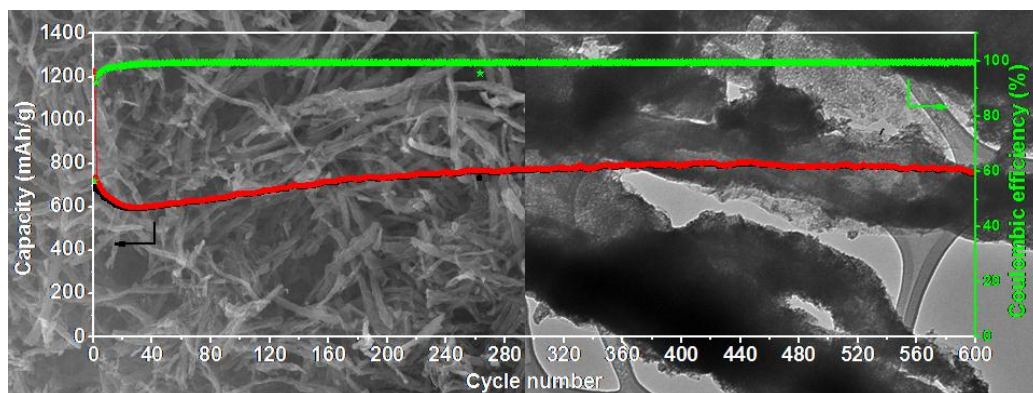


Executive Summary 3-D heterogeneously nanostructured thin-film electrodes were fabricated by using Ta_2O_5 nanotubes as a framework to support carbon onion-coated Fe_2O_3 nanoparticles along the surface of the nanotubes. Carbon onion layers function as microelectrodes to separate the two different metal oxides and form a nanoscale 3-D sandwich structure. In this way space-charge layers were formed at the phase boundaries, and it provides additional energy storage by

charge separation. These 3-D nanostructured thin-films deliver both excellent Li-ion battery properties (stabilized at 800 mAh cm⁻³) and supercapacitor (up to 18.2 mF cm⁻²) performance owing to the synergistic effects of the heterogeneous structure. Thus, Li-ion batteries and supercapacitors are successfully assembled into the same electrode, which is promising for next generation hybrid energy storage and delivery devices.

Yang, Y.; Peng, Z.; Wang, G.; Ruan, G.; Fan, X.; Li, L.; Fei, H.; Hauge, R. H.; Tour, J. M. “Three-Dimensional Thin Film for Lithium-Ion Batteries and Supercapacitors,” *ACS Nano*, **2014**, 8, 7279–7287. DOI: <http://dx.doi.org/10.1021/nn502341x>

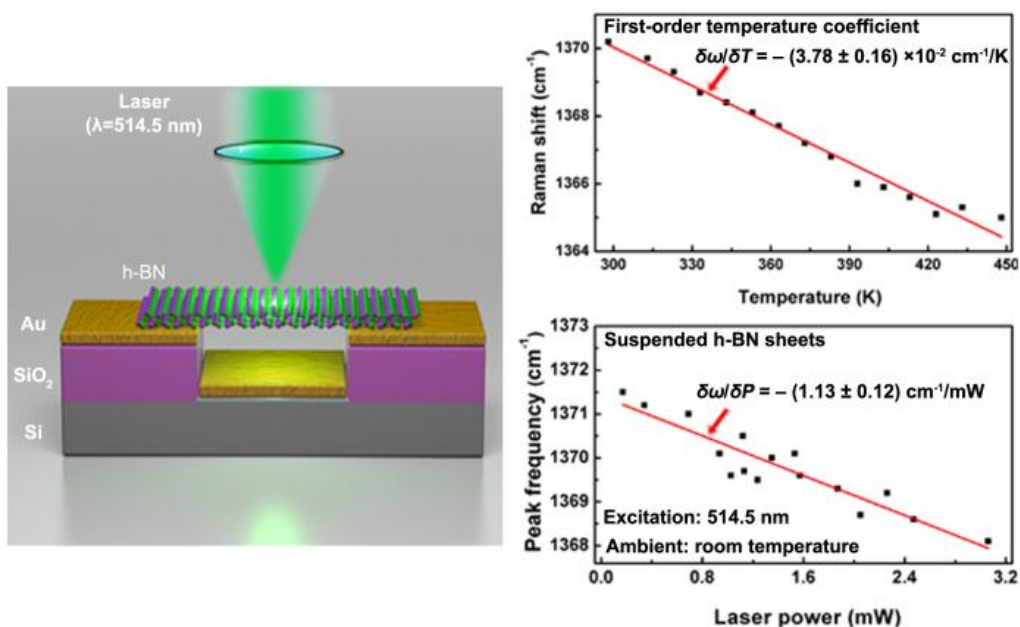
SnO₂-Reduced Graphene Oxide Nanoribbons as Anodes for Lithium Ion Batteries with Enhanced Cycling Stability



Executive Summary A nanocomposite material of SnO₂-reduced graphene oxide nanoribbons has been developed. In this composite, the reduced graphene oxide nanoribbons are uniformly coated by nanosized SnO₂ that formed a thin layer of SnO₂ on the surface. When used as anodes in lithium ion batteries, the composite shows outstanding electrochemical performance with the high reversible discharge capacity of 1027 mAh/g at 0.1 A/g after 165 cycles and 640 mAh/g at 3.0 A/g after 160 cycles with current rates varying from 0.1 to 3.0 A/g and no capacity decay after 600 cycles compared to the second cycle at a current density of 1.0 A/g. The high reversible capacity, good rate performance and excellent cycling stability of the composite are due to the synergistic combination of electrically conductive reduced graphene oxide nanoribbons and SnO₂. The method developed here is practical for the large-scale development of anode materials for lithium ion batteries.

Li, L.; Kovalchuk, A.; Tour, J. M. “SnO₂-Reduced Graphene Oxide Nanoribbons as Anodes for Lithium Ion Batteries with Enhanced Cycling Stability,” *Nano Res.* **2014**, 7, 1319-1326. DOI: <http://dx.doi.org/10.1007/s12274-014-0496-x>

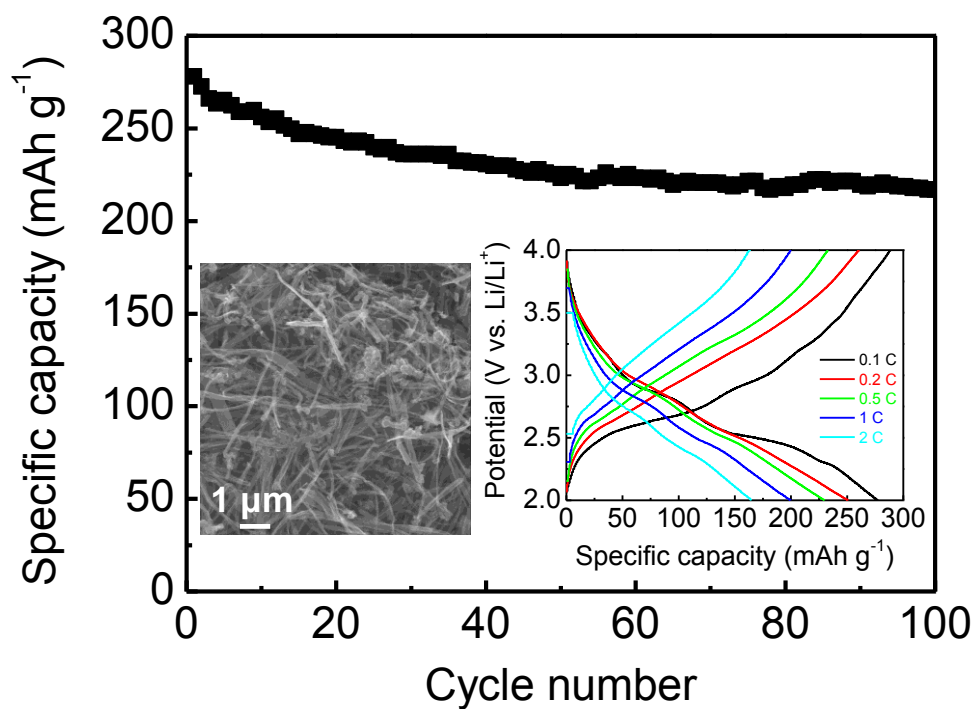
High thermal conductivity of suspended few-layer hexagonal boron nitride sheets



Executive Summary We report the experimental investigation of thermal conduction in suspended few-layer h-BN sheets using a noncontact micro-Raman spectroscopy method. The first-order temperature coefficients for monolayer (1L), bilayer (2L) and nine-layer (9L) h-BN sheets were found to be $-(3.41 \pm 0.12) \times 10^{-2}$, $-(3.15 \pm 0.14) \times 10^{-2}$ and $-(3.78 \pm 0.16) \times 10^{-2} \text{ cm}^{-1}/\text{K}$, respectively. The room-temperature thermal conductivity of few-layer h-BN sheets was found to be around $243 \text{ Wm}^{-1}\text{K}^{-1}$, which is comparable to that of bulk h-BN, indicating their potential use as important components to solve heat dissipation problems in thermal management configurations.

Zhou; H.; Zhu; J.; Liu; Z.; Yan; Z.; Fan; X.; Lin; J.; Wang, G.; Yan; Q.; Yu; T.; Ajayan; P. M.; Tour, J. M. "High Thermal Conductivity of Suspended Few-Layer Hexagonal Boron Nitride Sheets," *Nano Res.*, **2014**, 7, 1232-1240. DOI: <http://dx.doi.org/10.1007/s12274-014-0486-z>

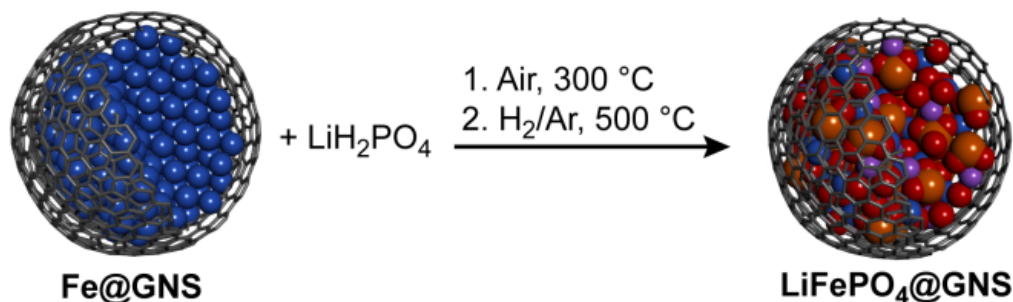
Graphene Nanoribbon/V₂O₅ Cathodes in Lithium-Ion Batteries



Executive Summary Nanocrystalline V₂O₅ particles were successfully entrapped by graphene nanoribbons (GNRs) derived from unzipped carbon nanotubes. The electrical conductivity of V₂O₅ nanoparticles was enhanced after introducing the GNRs. The 3-dimensional conductive framework in the composites plays a significant role in improving the rate performance and cyclability of the material when used as a cathode in lithium-ion batteries. By tailoring the mass ratio between the GNRs and the V₂O₅ nanoparticles, the fabricated composites can deliver a high capacity of 278 mAh g⁻¹ at 0.1 C which is closed to its theoretical value, while a capacity of 165 mAh g⁻¹ can be maintained at 2 C. The delivered capacity at 0.1 C can maintain 78% of its initial capacity after 100 cycles.

Yang, Y.; Li, L.; Fei, H.; Peng, Z.; Ruan, G.; Tour, J. M. "Graphene Nanoribbon/V₂O₅ Cathodes in Lithium-Ion Batteries," *ACS Appl. Mater. Interfaces* **2014**, 6, 9590–9594, DOI: <http://dx.doi.org/10.1021/am501969m>

LiFePO₄ Nanoparticles Encapsulated in Graphene Nanoshells for High-Performance Lithium-Ion Battery Cathodes



Executive Summary LiFePO₄ encapsulated in graphene nanoshells (LiFePO₄@GNS) nanoparticles were synthesized by solid state reaction between graphene-coated Fe nanoparticles and LiH₂PO₄. The resulting nanocomposite was demonstrated to be a superior lithium-ion battery cathode with improved cycle and rate performances.

Fei, H.; Peng, Z.; Yang, Y.; Li, L.; Raji, A.-R. O.; Samuel, E. L. G.; Tour, J. M. "LiFePO₄ Nanoparticles Encapsulated in Graphene Nanoshells for High-Performance Lithium-Ion Battery Cathodes," *Chem. Commun.*, **2014**, 50, 7117-7119. DOI: <http://dx.doi.org/10.1039/C4CC02123A>

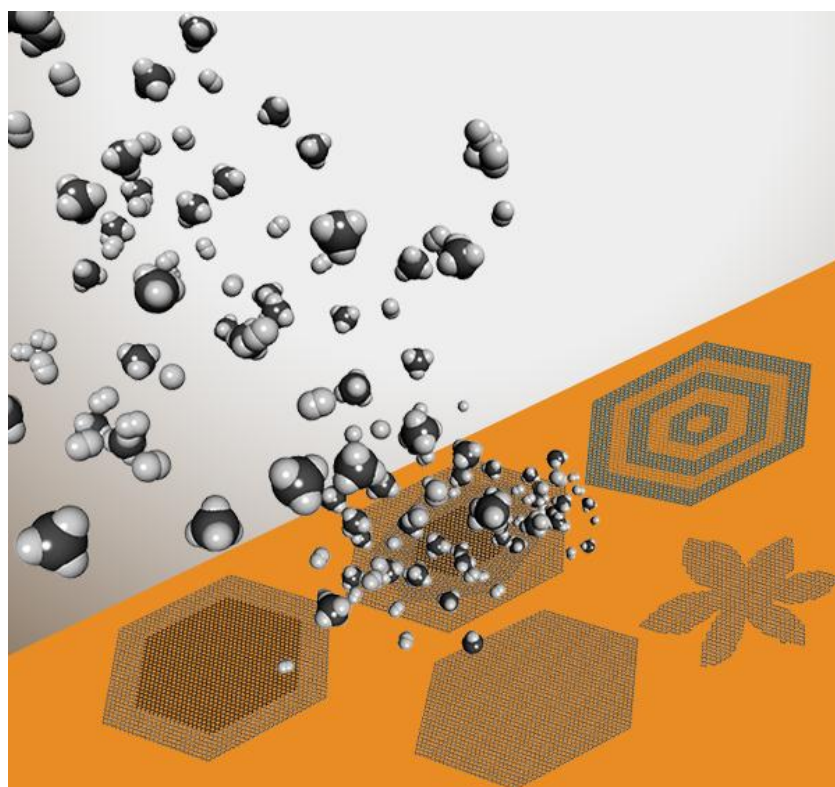
Mechanism of Graphene Oxide Formation



Executive Summary Despite intensive research, the mechanism of graphene oxide (GO) formation remains unclear. The role of interfacial interactions between solid graphite and the liquid reaction medium, and transport of the oxidizing agent into the graphite, have not been well-addressed. In this work we show that formation of GO from graphite constitutes three distinct independent steps. The reaction can be stopped at each step and the corresponding intermediate products can be isolated, characterized and stored under appropriate conditions. The first step is conversion of graphite into a stage-1 graphite intercalation compound (GIC). The second step is conversion of the stage-1 GIC into oxidized graphite which we define as pristine graphite oxide (PGO). This step involves diffusion of the oxidizing agent into the preoccupied graphite galleries. This rate-determining step makes the entire process diffusive-controlled. The third step is conversion of PGO into conventional GO after exposure to water, which involves hydrolysis of covalent sulfates and loss of all interlayer registry.

Dimiev, A. M.; Tour, J. M. "Mechanism of Graphene Oxide Formation," *ACS Nano* **2014**, 8, 3060–3068. DOI: <http://dx.doi.org/10.1021/nm500606a>

Chemical Vapor Deposition of Graphene Single Crystals (A Review)



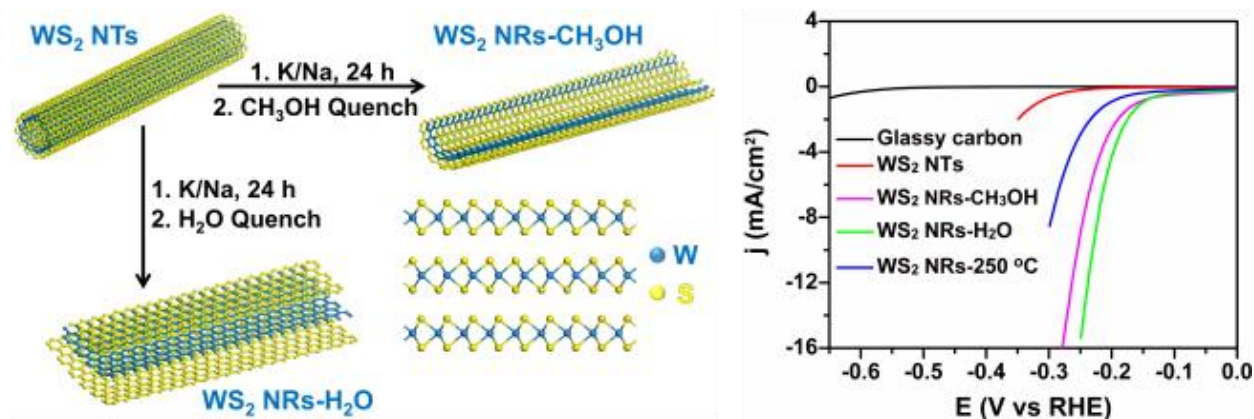
Executive Summary As a two-dimensional (2D) sp^2 -bonded carbon allotrope, graphene has attracted enormous interest over the last decade due to its unique properties, such as ultrahigh electron mobility, uniform broadband optical absorption and high tensile strength. In the initial research, graphene was isolated from natural graphite, and limited to small sizes and low yields. Recently developed chemical vapor deposition (CVD) techniques have emerged as an important method for the scalable production of large-size and high-quality graphene for various applications. However, CVD-derived graphene is polycrystalline and demonstrates degraded properties induced by grain boundaries. Thus, the next critical step of graphene growth relies on the synthesis of large graphene single crystals.

In this review, we first discuss graphene grain boundaries and their influence on graphene's properties. Mechanical and electrical behaviors of CVD-derived polycrystalline graphene are greatly reduced when compared to that of exfoliated graphene. We then review four representative pathways of pretreating Cu substrates to make millimeter-sized monolayer graphene grains: electrochemical polishing and high-pressure annealing of Cu substrate, adding of additional Cu enclosures, melting and resolidifying Cu substrates, and oxygen-rich Cu substrates. Due to these pretreatments, the nucleation site density on Cu substrates is greatly reduced, resulting in hexagonal-shaped graphene grains that show increased grain domain size and comparable electrical properties as to exfoliated graphene. Also, the properties of graphene can be engineered by its shape, thickness and spatial structure. Thus, we further discuss recently developed methods of making graphene grains with special spatial structures, including snowflakes, six-lobed flowers, pyramids and hexagonal graphene onion rings. The fundamental growth mechanism and practical applications of these well-shaped graphene structures should be interesting topics and deserves more attention in the near future. Following that, recent efforts in fabricating large single-crystal monolayer graphene on other metal substrates, including Ni, Pt and Ru, are also described. The differences in growth conditions reveal different growth mechanisms on these metals. Another key challenge for graphene growth is to make graphene single crystals on insulating substrates, such as h-BN, SiO_2 and ceramic. The recently developed plasma-enhanced CVD method can be used to directly synthesize graphene single crystals on h-BN substrates and is described in this Account as well.

To summarize, recent research in synthesizing millimeter-sized monolayer graphene grains with different pretreatments, graphene grain shapes, metal catalysts and substrates is reviewed. Although great advancements have been achieved in CVD synthesis of graphene single crystals, potential challenges still exist, such as the growth of wafer-sized graphene single crystals to further facilitate the fabrication of graphene-based devices, as well as a deeper understanding of graphene growth mechanisms and growth dynamics in order to make graphene grains with precisely controlled thicknesses and spatial structures.

Yan, Z.; Peng, Z.; Tour, J. M. “Chemical Vapor Deposition of Graphene Single Crystals,” *Acc. Chem. Res.* **2014**, 47, 1327–1337. DOI: <http://dx.doi.org/10.1021/ar4003043>

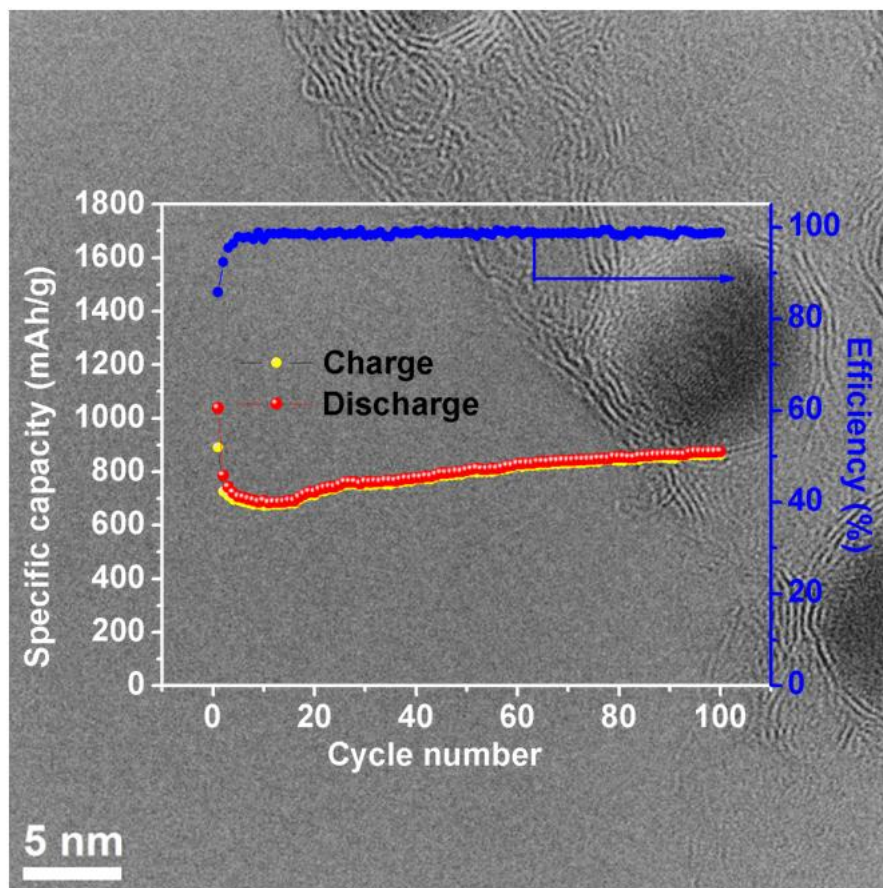
Enhanced Electrocatalysis for Hydrogen Evolution Reactions from WS₂ Nanoribbons



A facile route was developed to boost the electrocatalytic activity of WS₂ by chemically unzipping WS₂ nanotubes to form WS₂ nanoribbons (NRs) with increased edge content. Analysis indicates that hydrogen evolution reaction activity is strongly associated with the number of exposed active edge sites. The formation of WS₂ NRs is another effective route for controlling the electrochemical properties of the two-dimensional dichalcogenides, enabling their application to electrocatalysis.

Lin, J., Peng, Z., Wang, G., Zakhidov, D., Larios, E., Yacaman, M. J.; Tour, J. M. “Enhanced Electrocatalysis for Hydrogen Evolution Reactions from WS₂ Nanoribbons,” *Adv. Energy Mater.* **2014**, 1301875. DOI: <http://dx.doi.org/10.1002/aenm.201301875>

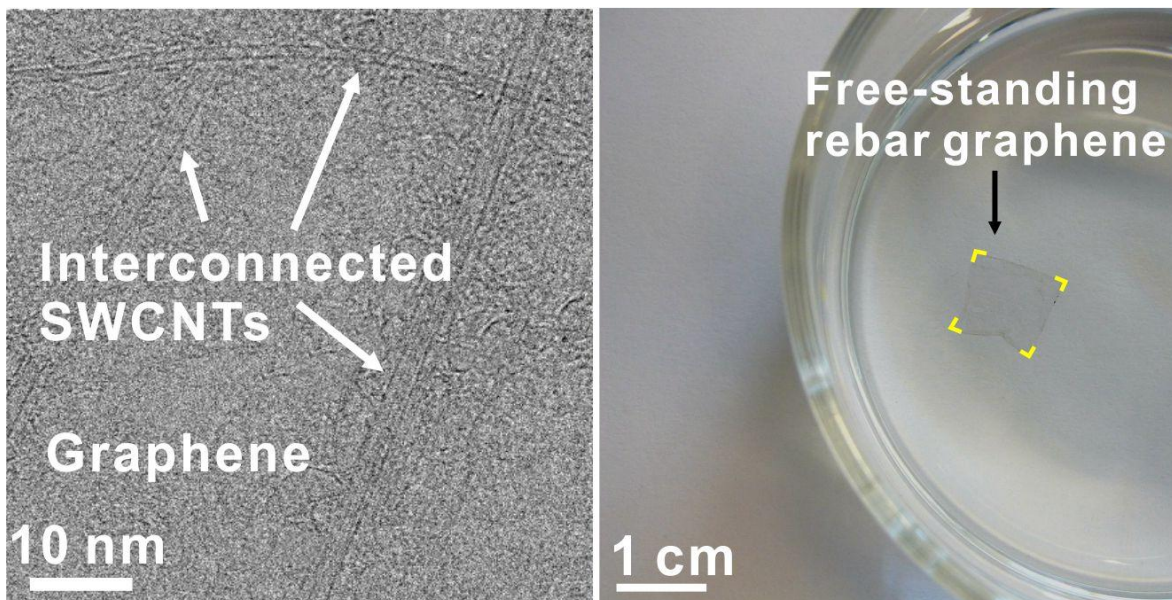
Preparation of carbon-coated iron oxide nanoparticles dispersed on graphene sheets and applications as advanced anode materials for lithium-ion batteries



Executive Summary We report a novel chemical vapor deposition (CVD) based strategy to synthesize carbon-coated Fe₂O₃ nanoparticles dispersed on graphene sheets (Fe₂O₃@C@G). Graphene sheets with high surface area and aspect ratio are chosen as space restrictor to prevent the sintering and aggregation of nanoparticles during high temperature treatments (800 °C). In the resulting nanocomposite, each individual Fe₂O₃ nanoparticle (5 to 20 nm in diameter) is uniformly coated with a continuous and thin (2 to 5 layers) graphitic carbon shell. Further, the core-shell nanoparticles are evenly distributed on graphene sheets. When used as anode materials for lithium ion batteries, the conductive-additive-free Fe₂O₃@C@G electrode shows outstanding Li⁺ storage properties with large reversible specific capacity (864 mAh/g after 100 cycles), excellent cyclic stability (120% retention after 100 cycles at 100 mA/g), high Coulombic efficiency (~ 99%), and good rate capability.

Fei, H.; Peng, Z.; Li, L.; Yang, Y.; Lu, W.; Samuel, E. L. G.; Fan, X.; Tour, J. M. "Preparation of Carbon-Coated Iron Oxide Nanoparticles Dispersed on Graphene Sheets and Applications as Advanced Anode Materials for Lithium-Ion Batteries," *Nano Research* **2014**, 7, 502-510. DOI: <http://dx.doi.org/10.1007/s12274-014-0416-0>

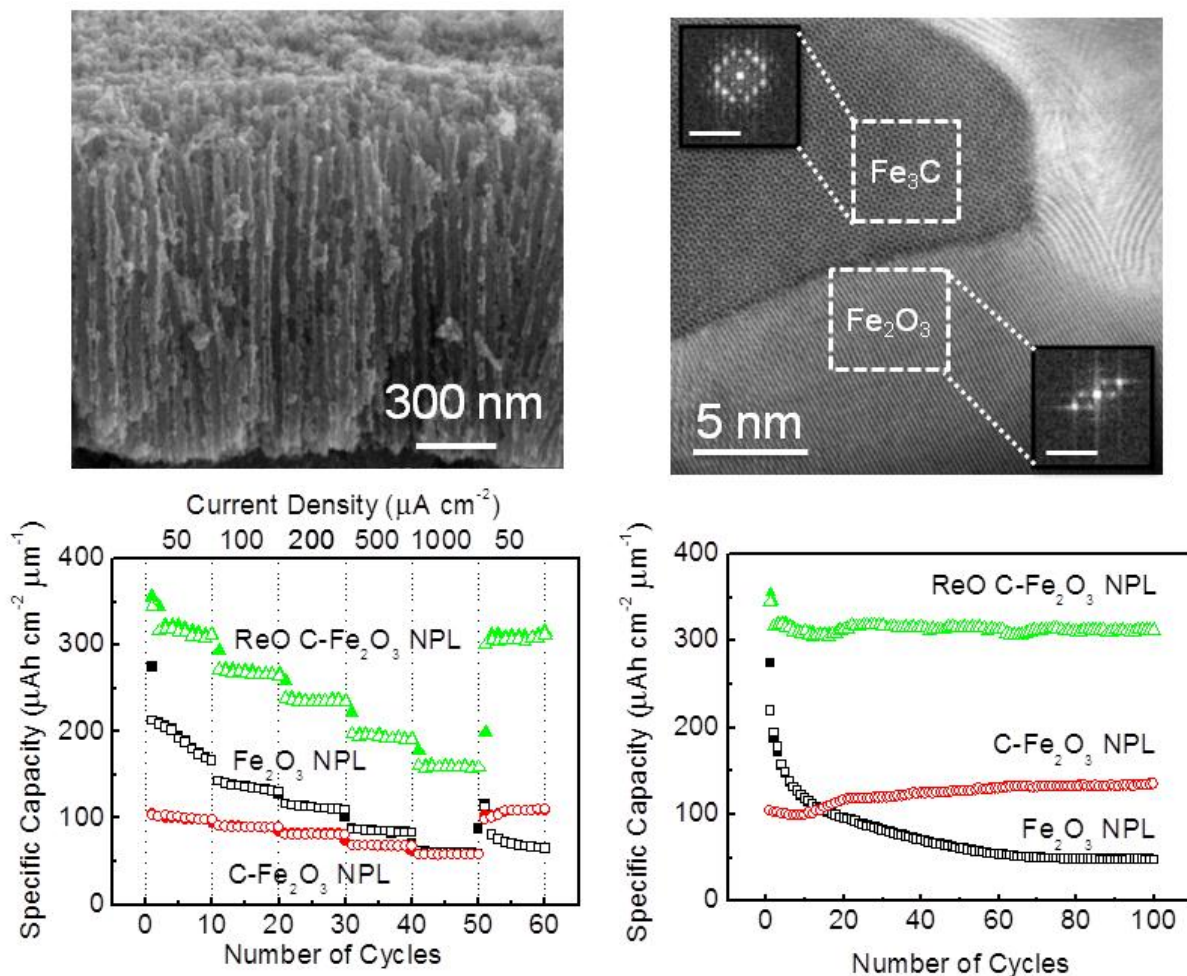
Rebar Graphene



Executive Summary As the cylindrical sp^2 -bonded carbon allotrope, carbon nanotubes (CNTs) have been widely used to reinforce bulk materials such as polymers, ceramics and metals. However, both the concept demonstration and the fundamental understanding on how 1D CNTs reinforce atomically thin 2D layered materials, like graphene, are still absent. Here we demonstrate the successful synthesis of CNT-toughened graphene by simply annealing functionalized CNTs on Cu foils without needing to introduce extraneous carbon sources. The CNTs act as reinforcing bar (rebar), toughening the graphene through both π - π stacking domains and covalent bonding where the CNTs partially unzip and form a seamless 2D conjoined hybrid as revealed by aberration-corrected scanning transmission electron microscopy (STEM) analysis. This is termed rebar-graphene. Rebar graphene can be free-standing on water and transferred onto target substrates without needing a polymer-coating due to the rebar effects of the CNTs. The utility of rebar graphene sheets as flexible all-carbon transparent electrodes is demonstrated. The in-plane marriage of 1D nanotubes and 2D layered materials might herald an electrical and mechanical union that extends beyond carbon chemistry.

Yan, Z.; Peng, Z.; Casillas, G.; Lin, J.; Xiang, C.; Zhou, H.; Yang, Y.; Ruan, G.; Raji, A.-R. O.; Samuel, E. L. G.; Hauge, R. H.; Yacaman, M. J.; Tour, J. M. "Rebar Graphene," *ACS Nano*, **2014**, 8, 5061-5068. DOI: <http://dx.doi.org/10.1021/nm501132n>

3-Dimensional Nanoporous $\text{Fe}_2\text{O}_3/\text{Fe}_3\text{C}$ -Graphene Heterogeneous Thin Films for Lithium-Ion Batteries

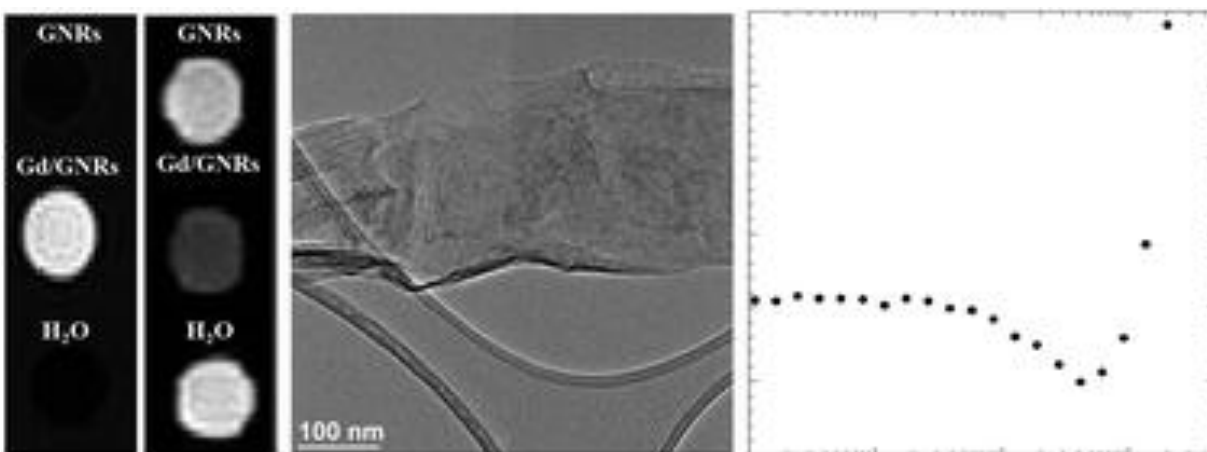


Executive Summary 3-Dimensional self-organized nanoporous thin films integrated into a heterogeneous $\text{Fe}_2\text{O}_3/\text{Fe}_3\text{C}$ -graphene structure were fabricated using chemical vapor deposition. Few-layer graphene coated on the nanoporous thin film was used as a conductive passivation layer and Fe_3C was introduced to improve capacity retention and stability of the nanoporous layer. A possible interfacial lithium storage effect was anticipated to provide additional charge storage in the electrode. These nanoporous layers, when used as an anode in lithium ion batteries,

deliver greatly enhanced cyclability and rate capacity compared with pristine Fe_2O_3 : a specific capacity of $356 \mu\text{Ah cm}^{-2} \mu\text{m}^{-1}$ (3560 mAh cm^{-3} or $\sim 1118 \text{ mAh g}^{-1}$) obtained at discharge current density of $50 \mu\text{A cm}^{-2}$ ($\sim 0.17 \text{ C}$) with 88% retention after 100 cycles and $165 \mu\text{Ah cm}^{-2} \mu\text{m}^{-1}$ (1650 mAh cm^{-3} or $\sim 518 \text{ mAh g}^{-1}$) obtained at discharge current density of $1000 \mu\text{A cm}^{-2}$ ($\sim 6.6 \text{ C}$) for 1000 cycles were achieved. Meanwhile an energy density of $294 \mu\text{Wh cm}^{-2} \mu\text{m}^{-1}$ (2.94 Wh cm^{-3} or $\sim 924 \text{ Wh kg}^{-1}$) and power density of $584 \mu\text{W cm}^{-2} \mu\text{m}^{-1}$ (5.84 W cm^{-3} or $\sim 1834 \text{ W kg}^{-1}$) were also obtained which may make these thin film anode promising as power supply for micro- or even nano-sized portable electronic devices.

Yang, Y.; Fan, X.; Casillas, G.; Peng, Z.; Ruan, G.; Wang, G.; Yacaman, M. J.; Tour, J. M. "Three-Dimensional Nanoporous $\text{Fe}_2\text{O}_3/\text{Fe}_3\text{C}$ Graphene Heterogeneous Thin Films for Lithium-Ion Batteries," *ACS Nano* **2014**, 8, 3939-3946. DOI: <http://dx.doi.org/10.1021/nm500865d>

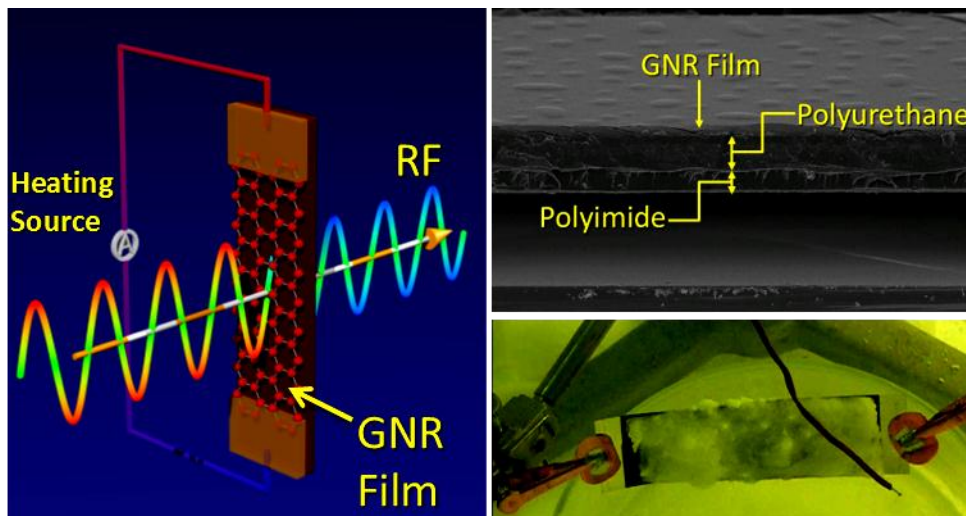
Enhanced MRI relaxivity of aquated Gd^{3+} ions by carboxyphenylated water-soluble graphene nanoribbons



Executive Summary Graphene has emerged as a promising material for many different applications. In the present study, we demonstrate that highly water-soluble graphene nanoribbons solubilized by carboxyphenylated substituents and conjugated to aquated Gd^{3+} ions can serve as a high-performance contrast agent (CA) for applications in T_1 - and T_2 -weighted magnetic resonance imaging (MRI) with relaxivity ($r_{1,2}$) values outperforming currently-available clinical CAs by up to 16 times for r_1 and 21 times for r_2 .

Gizzatov, A.; Keshishian, V.; Guven, A.; Dimiev, A. M.; Qu, F.; Muthupillai, R.; Decuzzi, P.; Bryant, R. G.; Tour, J. M.; Wilson, L. J. "Enhanced MRI Relaxivity of Aquated Gd^{3+} Ions by Carboxyphenylated Water-Dispersed Graphene Nanoribbons," *Nanoscale* **2014**, 6, 3059-3063. DOI: <http://dx.doi.org/10.1039/C3NR06026H>

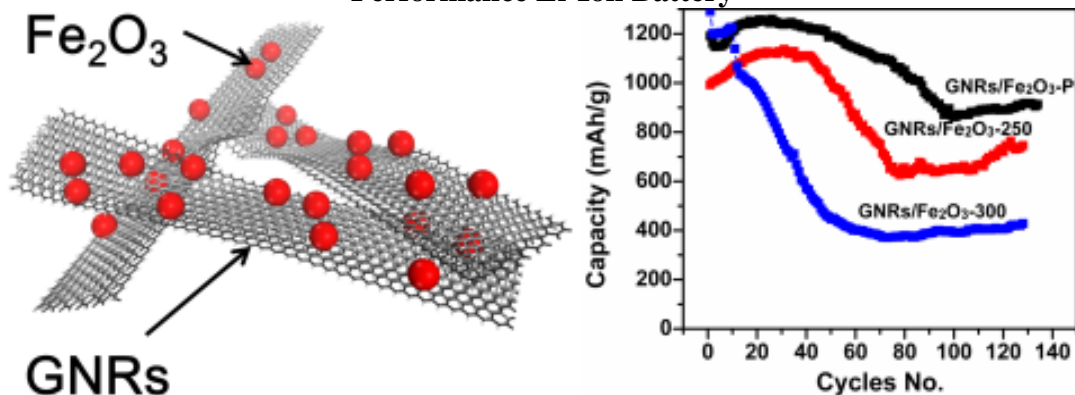
Radiofrequency Transparent, Electrically Conductive Graphene Nanoribbon Thin Films as De-icing Heating Layers



Executive Summary De-icing heating layers are frequently used in covers of large radiofrequency (RF) equipment, such as radar, to remove ice that could damage the structures or make them unstable. Typically the de-icers are made using a metal framework and inorganic insulator; commercial resistive heating materials are often non-transparent to RF waves. The preparation of sub-skin-depth thin film, whose thickness is very small relative to RF skin (or penetration) depth, is the key to minimizing RF absorption. The skin depth of typical metals is on the order of a micrometer at GHz frequency range. As a result, it is very difficult for conventional conductive materials (such as metals) to form large area sub-skin-depth films. In this report, we disclose a new de-icing heating layer composite made using graphene nanoribbons (GNRs). We demonstrate that the GNR film is thin enough to permit RF transmission. This metal-free, ultralight, robust, and scalable graphene-based RF-transparent conductive coating could significantly reduce the size and cost of de-icing coatings for RF equipment covers. This is important in many aviation and marine applications. This is a demonstration of the efficacy and applicability of GNRs to afford performances unattainable by conventional materials.

Volman, V.; Zhu, Y.; Raji, A.-R., O.; Genorio, B.; Lu, W.; Xiang, C.; Kittrell, C.; Tour, J. M. "Radio-Frequency-Transparent, Electrically Conductive Graphene Nanoribbon Thin Films as Deicing Heating Layers," *ACS Appl. Mater. Interfaces*, **2014**, 6, 298-304. DOI: <http://dx.doi.org/10.1021/am404203y>

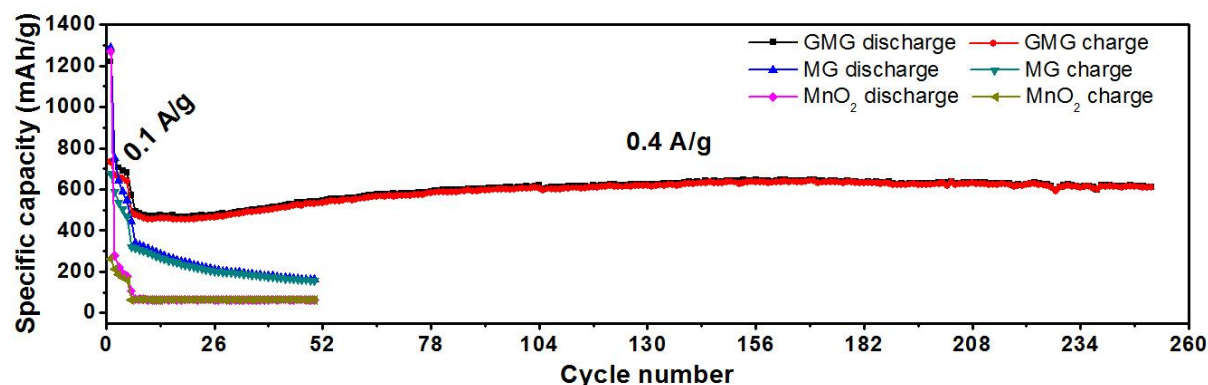
Iron Oxide Nanoparticle and Graphene Nanoribbon Composite Anode for High Performance Li-Ion Battery



Executive Summary A facile and scalable synthesis route to GNRs/Fe₂O₃ composite was developed as anode material for LIBs. The unique structures of GNRs with high electrical conductivity and the enhanced vacancy of iron oxide NPs leads to excellent electrochemical performance. The fabricated anode shows a reversible capacity of 1190 mAh/g and retains 910 mAh/g after 134 cycles with high rate performance of 544 mAh/g at a rate of 2 A/g.

Lin, J.; Raji, A.-R., O.; Nan, K.; Peng, Z.; Yan, Z.; Samuel, E. L. G.; Natelson, D.; Tour, J. M. "Iron Oxide Nanoparticle and Graphene Nanoribbon Composite as an Anode Material for High-Performance Li-Ion Batteries," *Adv. Funct. Mater.* **2013**, 24, 2044–2048. DOI: <http://dx.doi.org/10.1002/adfm.201303023>

Graphene-Wrapped MnO₂-Graphene Nanoribbons as Anode Materials for High Performance Lithium Ion Batteries



Executive Summary A facile and cost-effective approach to the fabrication of a hierarchical nanocomposite material of graphene-wrapped MnO₂-graphene nanoribbons (GMG) has been

developed. The resulting composite has a high specific capacity and an excellent cycling stability due to the synergistic combination of electrically conductive graphene, graphene nanoribbons, and MnO₂.

Li, L.; Raji, A.-R. O.; Tour, J. M. “Graphene-Wrapped MnO₂ –Graphene Nanoribbons as Anode Materials for High-Performance Lithium Ion Batteries,”*Adv. Mater.* **2013**, 25, 6298–6302. DOI: <http://dx.doi.org/10.1002/adma.201302915>

Coal as an abundant source of graphene quantum dots

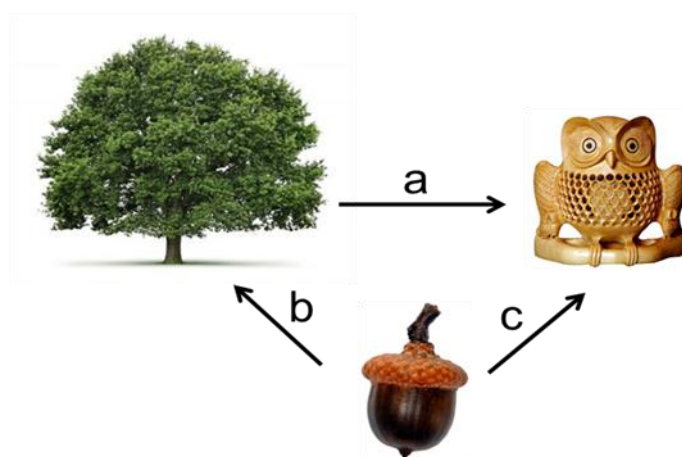


Executive Summary Coal is the most abundant and readily combustible energy resource being used worldwide. However, its structural characteristic creates a perception that coal is only useful for producing energy *via* burning. Here we report a facile approach to synthesize tunable graphene quantum dots from various types of coal, and establish that the unique coal structure has an advantage over pure sp²-carbon allotropes for producing quantum dots. The crystalline

carbon within the coal structure is easier to oxidatively displace than when pure sp^2 -carbon structures are used, resulting in nanometer-sized graphene quantum dots with amorphous carbon addends on the edges. The synthesized graphene quantum dots, produced in up to 20% isolated yield from coal, are soluble and fluorescent in aqueous solution, providing promise for applications in areas such as bioimaging, biomedicine, photovoltaics and optoelectronics, in addition to being inexpensive additives for structural composites.

Ye, R.; Xiang, C.; Lin, J.; Peng, Z.; Huang, K.; Yan, Z.; Cook, N. P.; Samuel, E. L. G.; Hwang, C.-C.; Ruan, G.; Ceriotti, G.; Raji, A.-R. O.; Martí, A. A.; Tour, J. M. "Coal as an Abundant Source of Graphene Quantum Dots," *Nature Commun.* **2013**, 4:2943, 1-6. DOI: <http://dx.doi.org/10.1038/ncomms3943>

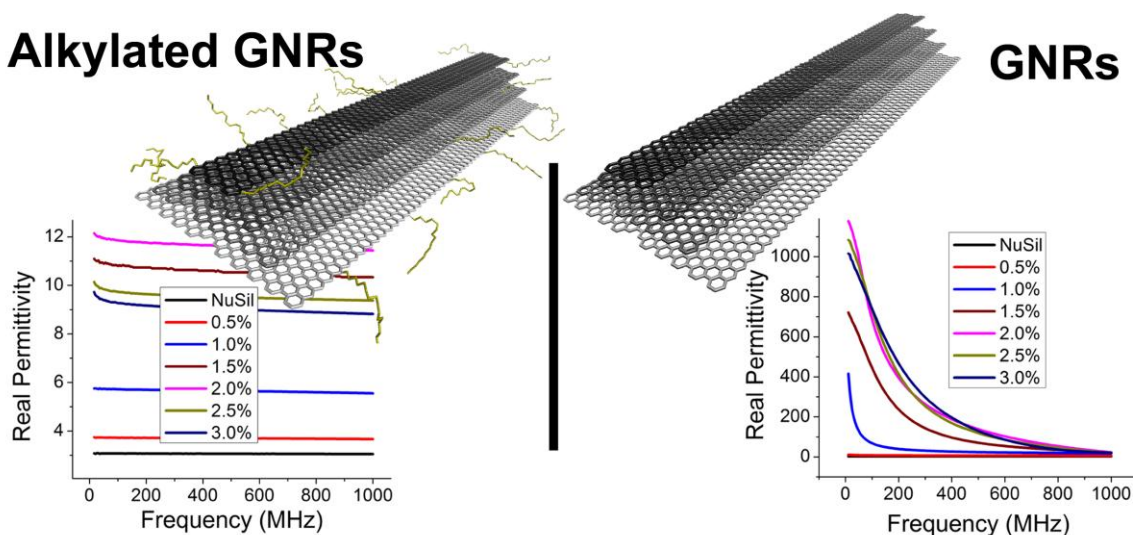
Top-Down versus Bottom-Up Fabrication of Graphene-Based Electronics



Executive Summary Graphene electronic devices can be made by top-down (TD) or bottom-up (BU) approaches. This Perspective defines and explains those two approaches and discusses the advantages and limitations of each, particularly in the context of graphene fabrication. It is further exemplified using graphene nanoribbons as the prototypical graphene structure that can be prepared using either a TD or BU approach. The TD approach is well-suited for placement of large arrays of devices on a chip using standard patterning tools. However, the TD approach severely compromises the edges of the graphene since present fabrication tools are coarse relative to the ~ 0.1 nm definition of a C-C bond. The BU approach can afford exquisite control of the graphene edges; however, placing the structures, *en mass*, in the locations of interest is often impossible. Also, using the BU approach, it can be very difficult to make device structures long enough for integration with TD-derived probe electrodes. Specific examples are shown, along with an outlook for optimization of future graphene devices in order to capitalize upon the advantages of both TD and BU fabrication methodologies.

Tour, J. M. "Top-Down versus Bottom-Up Fabrication of Graphene-Based Electronics," *Chem. Mater.* **2014**, 26, 163-171. DOI: <http://dx.doi.org/10.1021/cm402179h>

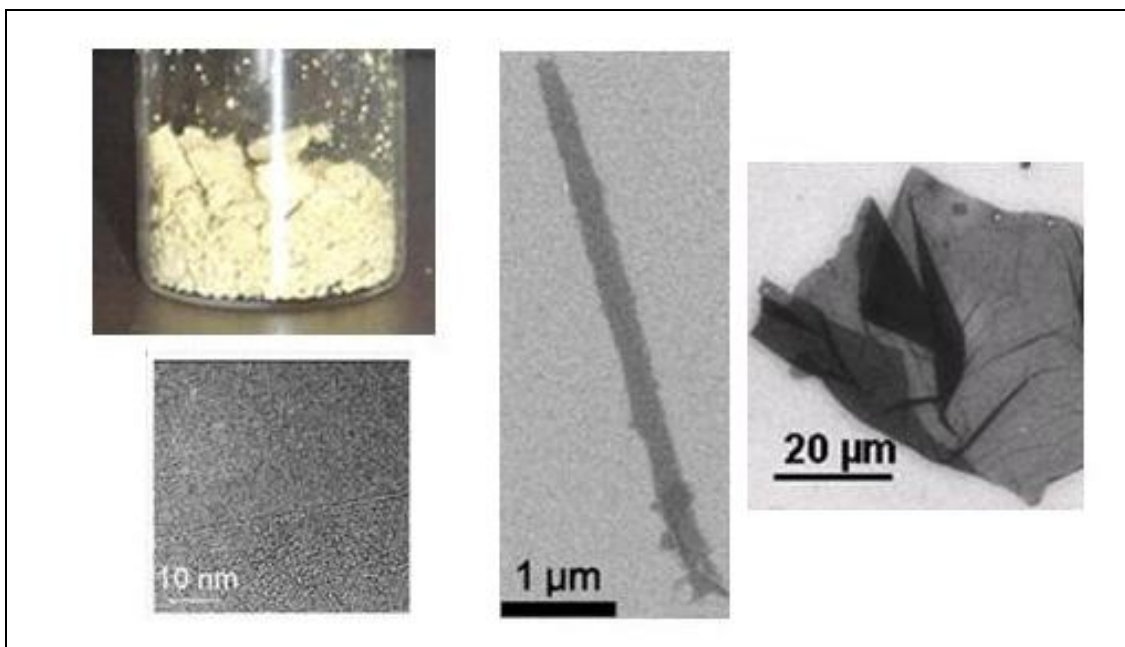
Permittivity of Dielectric Composite Materials Comprising Graphene Nanoribbons. The Effect of Nanostructure



Abstract New light-weight, flexible dielectric composite materials were fabricated by incorporation of several new carbon nanostructures into a dielectric host matrix. Both permittivity and loss tangent values of the resulting composites were widely altered by varying the type and content of the conductive filler. The dielectric constant was tuned from moderate to very high values, while the corresponding loss tangent changed from ultra-low through extremely high. The data exemplifies that nano-scale changes in the structure of the conductive filler results in dramatic changes in the dielectric properties of composites. A microcapacitor model most explains the behavior of the dielectric composites.

Dimiev, A.; Zakhidov, D.; Genorio, B.; Oladimeji, K.; Crowgey, B.; Kempel, L.; Rothwell, E. J.; Tour, J. M. "Permittivity of Dielectric Composite Materials Comprising Graphene Nanoribbons. The Effect of Nanostructure," *ACS Appl. Mater. Interfaces*, **2013**, 5, 7567–7573. DOI: <http://dx.doi.org/10.1021/am401859j>

Graphene: Powder, Flakes, Ribbons and Sheets (A Review)



Executive Summary Graphene's unique physical and electrical properties (high tensile strength, Young's modulus, electron mobility and thermal conductivity) have led to its nickname of "super carbon." Graphene research involves the study of several different physical forms of the material: powders, flakes, ribbons and sheets and others not yet named or imagined. Within those forms, graphene can include a single layer, two layers or ≤ 10 sheets of sp^2 carbon atoms. The chemistry and applications available with graphene depend on both the physical form of the graphene and the number of layers in the material. Therefore the available permutations of graphene are numerous and we will discuss a subset of this work, covering some of our research on the synthesis and/or use of many of the different physical and layered forms of graphene.

Initially we worked with commercially available graphite, with which we extended diazonium chemistry developed to functionalize single-walled carbon nanotubes to produce graphitic materials. These structures were soluble in common organic solvents and were better dispersed in composites. We developed an improved synthesis of graphene oxide (GO) and explored how the workup protocol for the synthesis of GO can change the electronic structure and chemical functionality of the GO product. We also developed a method to remove graphene layers one-

by-one from flakes. These powders and sheets of GO can serve as fluid loss prevention additives in drilling fluids for the oil industry.

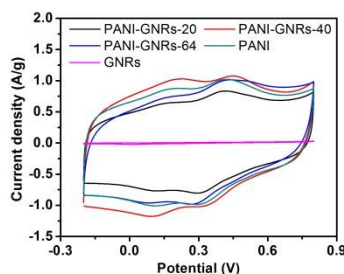
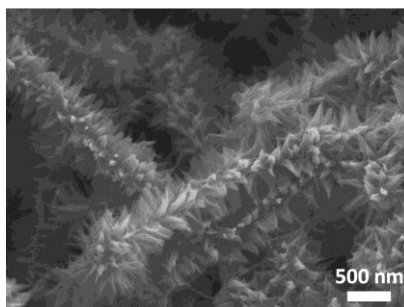
Graphene nanoribbons (GNRs) combine small width with long length, producing valuable electronic and physical properties. We developed two complementary syntheses of GNRs from multiwalled carbon nanotubes: one simple oxidative method that produces GNRs with some defects and one reductive method that produces GNRs that are less defective and more electrically conductive. These GNRs can be used in low-loss, high permittivity composites, as conductive reinforcement coatings on Kevlar fibers and in the fabrication of large area transparent electrodes.

Using solid carbon sources such as polymers, food, insects and waste, we can grow monolayer and bilayer graphene directly on metal catalysts, and carbon-sources containing nitrogen can produce nitrogen-doped graphene. The resulting graphene can be transferred to other surfaces, such as metal grids, for potential use in transparent touch screens for applications in personal electronics and large area photovoltaic devices. Because the transfer of graphene from one surface to another can lead to defects, low yields and higher costs, we have developed methods for growing graphene directly on the substrates of interest. We can also produce patterned graphene to make GNRs or graphane/graphene superlattices within a single sheet. These superlattices could have multiple functions for use in sensors and other devices.

This Account only touches upon this burgeoning area of materials chemistry, and the field will continue to expand as researchers imagine new forms and applications of graphene.

James, D. K.; Tour, J. M. "Graphene: Powder, Flakes, Ribbons, and Sheets," *Acc. Chem. Res.* **2013**, 46, 2307–2318. DOI: <http://dx.doi.org/10.1021/ar300127r>

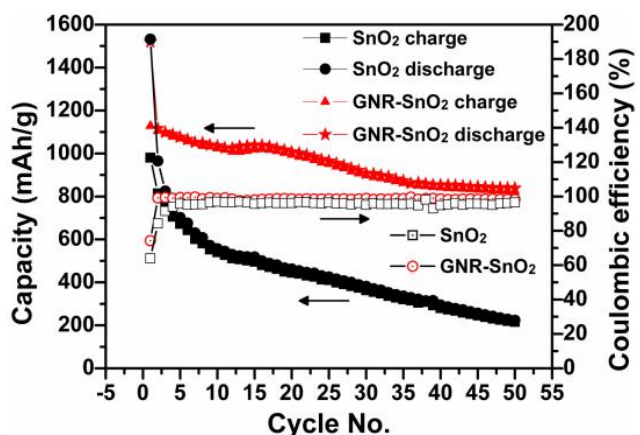
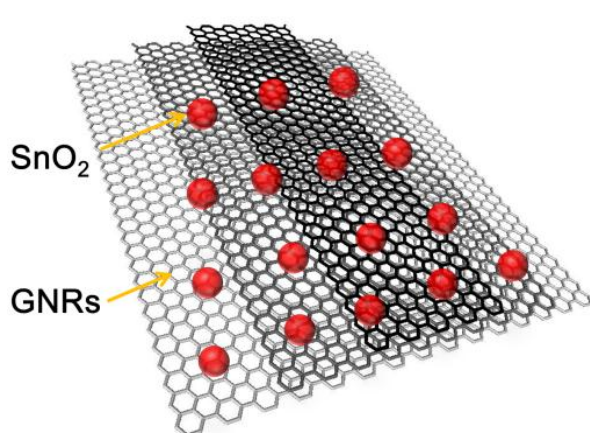
Nanocomposite of Polyaniline Nanorods Grown on Graphene Nanoribbons for Highly Capacitive Pseudocapacitors



Executive Summary A facile and cost-effective approach to the fabrication of a nanocomposite material of polyaniline (PANI) and graphene nanoribbons (GNRs) has been developed. The morphology of the composite was characterized by scanning electron microscopy, transmission electron microscopy, X-ray photoelectron microscopy and X-ray diffraction analysis. The resulting composite has a high specific capacitance of 340 F/g and stable cycling performance with 90% capacitance retention over 4200 cycles. The high performance of the composite results from the synergistic combination of electrically conductive GNRs and highly capacitive PANI. The method developed here is practical for large-scale development of pseudocapacitor electrodes for energy storage.

Li, L.; Raji, A.-R. O.; Fei, H.; Yang, Y.; Samuel, E. L. G.; Tour, J. M. "Nanocomposite of Polyaniline Nanorods Grown on Graphene Nanoribbons for Highly Capacitive Pseudocapacitors," *ACS Appl. Mater. Interfaces* **2013**, 5, 6622–6627. DOI: <http://dx.doi.org/10.1021/am4013165>

Graphene Nanoribbon and Nanostructured SnO₂ Composite Anodes for Lithium Ion Batteries



Executive Summary A composite made from graphene nanoribbons (GNRs) and tin oxide (SnO₂) nanoparticles (NPs) is synthesized and used as the anode material for lithium ion batteries (LIBs). The conductive GNRs, prepared using sodium/potassium unzipping of multiwall carbon nanotubes, can boost the lithium storage performance of SnO₂ NPs. The composite, as an anode material for LIBs, exhibits reversible capacities of over 1520 mAh/g and 1130 mAh/g for the first discharge and charge, respectively, which is more than the theoretical capacity of SnO₂. The reversible capacity retains ~ 825 mAh/g at a current density of 100 mA/g with a Coulombic efficiency of 98% after 50 cycles. Further, the composite shows good power performance with a reversible capacity of ~580 mAh/g at the current density of 2 A/g. The high capacity, good power performance and retention can be attributed to uniformly distributed SnO₂ NPs along the

high-aspect-ratio GNRs. The GNRs act as conductive additives that buffer the volume changes of SnO₂ during cycling. This work provides a starting point for exploring the composites made from GNRs and other transition metal oxides for lithium storage applications.

Lin, J.; Peng, P.; Xiang, C.; Ruan, G.; Yan, Z.; Natelson, D. Tour, J. M. “Graphene Nanoribbon and Nanostructured SnO₂ Composite Anodes for Lithium Ion Batteries,” *ACS Nano*, **2013**, 7, 6001–6006. DOI: <http://dx.doi.org/10.1021/nn4016899>